Bernardo Pereira Madeira

⟨Bachelor of Science in Micro and Nanotechnologies Engineering ⟩

Characterization of MEMS Coriolis Vibratory Gyroscopes

Dissertation submitted in partial fulfillment
of the requirements for the degree of

Master of Science in
Micro and Nanotechnologies Engineering

Adviser: Prof. Dr. Michael Kraft
Full Professor, ESAT/MNS – KU Leuven

Co-adviser: Prof. Dr. Luís Miguel Nunes Pereira
Associate Professor, DCM – FCT-NOVA

Examination Committee:

Chair: Prof. Dr. Rodrigo Ferrão de Paiva Martins, Full Professor, FCT-NOVA

Rapporteur: Prof. Dr. Hugo Filipe Silveira Gamboa, Associate Professor, FCT-NOVA

FACULDADE DE
CIÊNCIAS E TECNOLOGIA
UNIVERSIDADE NOVA DE LISBOA

⟨**April**⟩, ⟨**2021**⟩

Para os meus avós, Bernardo e Maria.

Acknowledgements

As I finish writing this master thesis, I cannot help but ponder everything that made this moment possible. This section will be thus dedicated to express my appreciation to everyone who helped me on this journey.

I am a firm believer that our actions have ripple effects on everyone and everything around us. Since the most interesting, devoted, caring people have surrounded me, it is natural that looking back; I cannot feel anything but gratitude. This love in both domains: professionally speaking – in my teachers, mentors and colleagues - and personally speaking – by my family and friends, marked me deeply.

Firstly, I would like to thank Professor Elvira Fortunato and Professor Rodrigo Martins for their vision by bringing to life an academic path dedicated to nanotechnology in Portugal. This degree, which has a little over a decade of existence, enabled the edification of the first graduates specialized in an area that so very often touches what made me fall in love with science: the possibility of turning science fiction into science reality and drive the world forward.

Secondly, I would like to thank my adviser, Professor Michael Kraft, for accepting me as a visiting master student in the Micro & Nano Systems research team. Prof. Kraft is one of the most knowledgeable, well-rounded, and motivating human beings I have worked under. To everyone who is part of the MNS team, my deepest thank you as well for making the environment the best one could hope for.

To Professor Luís Pereira, for being my co-adviser, and doing what every teacher should aim for: inciting curiosity in his students. Without the passion he brings to class, the MEMS area's interest would not be fostered, and I would not certainly be here. I would also like to thank every teacher of the Materials Science and Electronics Departments who shaped my knowledge and interests along the way.

To Chen Wang, for being an inspiring mentor as well as my daily supervisor. From time to time, while having conceptual discussions about the topics we were working on, I could not help but to think, "wow, he knows a lot" – I hope I can one day provoke the same feeling in other people. More than a mentor, Chen became my friend, and with time, also became "defeatable" on table tennis. He always pushed me to become better, and without him, my thesis and experience in KU Leuven would not be the same.

Next, I would like to thank my colleagues and friends who shared these past five years and a half with me. To my friends whom I shared a roof: would anything be the same if I did not meet you? The day to day can be very boring to most people, but not if you lived with Rui Esteves, Diogo Carvalho, José Bernabé, and Eduardo Encarnação. My memories with you will be cherished forever, and I genuinely mean that. I hope we never grow apart.

To Eduardo Oliveira, who seems like he was a part of my life way before university ever started. To Maria Rosa, it is effortless to look up to you in so many ways, so thank you for being my friend. To Diogo Lopes for sharing the Erasmus experience with me and creating a more extensive connection than if we had never dived headfirst into flying 3000km away from home for six months. To my girls Raquel Martins and Mariana Tomé for all the companionship and Tico coffee's. To Diogo "Alentejano", André Alves, Dmytro, Gui, Guida, Mariana Abreu, and many more than could never fit this page. If we ever shared something over these five years, I will inevitably hold dear our memories.

To my childhood friends in Cartaxo: We are a few years away from knowing each other for two decades! Your impact on my life is immeasurable in so many ways. What we share is something most people spend their whole life looking for – meaningful friendships. By this point, you have been part of my life for so long that I cannot imagine a future where you are not part of it. For all of that and much more, my sincere thank you for shaping me into who I am today: Rui, Semedo, Manel, Diogo Correia, Diogo Pedro, Cacelas, Honório, Sousa, Ospi, Crua, Cunha, Tiago, Chico, Esha and Bernardo Jarego.

Finalmente, nada disto seria possível sem os meus avós, Bernardo e Maria, que foram quase como segundos pais para nós. O meu imenso obrigado nunca será suficiente. Apesar do meu avô Bernardo já não estar presente, sei quão orgulhoso ele ficou por ter um neto engenheiro quando o meu irmão se graduou. Pois agora são dois. Para a minha avó, por ter o coração mais puro que já presenciei. Espero que me possas ver crescer por largos anos. Dedico-vos esta tese a ambos. Para a minha mãe e para o meu pai, obrigado pela devoção na educação dos vossos filhos. Nunca tomarei por garantido os sacrifícios e esforço que colocaram em nós. Se um dia for metade do que vocês foram enquanto pais, não preciso de ter medo de nada. Para o meu Tio Rui também, por estar sempre presente. Para o meu maninho David, por ser um exemplo a seguir em mais formas do que ele pensa e para a minha maninha Patrícia por me ter dado a possibilidade de a ver crescer. Espero que nunca nos separemos. Um restante obrigado a toda a família Pereira Madeira. Estando rodeado de amor, é natural que consiga atingir isto e muito mais.

"I have a difficult time seeing scientific results, (...) as anything but provisional approximations, to be enjoyed for a while and discarded as soon as better accounts become available. But skepticism about the current reach of science (...) does not imply diminished enthusiasm for the attempt to improve these provisional approximations." (António Damásio)

Abstract

A MEMS Gyroscope is a micromachined inertial sensor that can measure the angle of orientation or the angular rate of rotation. These devices have the potential to be used in high precision navigation, safety and consumer electronics applications.

Due to their complexity, MEMS Gyroscopes are prone to have imperfections that inhibit their full potential. By deeply characterizing these sensors, it is possible to validate fabrication methodologies, apply control circuit mechanisms, and design alternative mechanical structures that improve the performance.

In this project, a streamlined methodology for testing and characterizing these devices is presented and executed. Analysis to the obtained results is given. Aditionally, a prototype circuit was designed to operate the sensors in a closed-loop mode.

Two families of gyroscopes with different thickness were characterized - 40μm and 100μm. The devices presented low sensitivity thresholds due to the presence of a large quadrature error. A phase sensitive demodulation solution was provided to eliminate this noise source. The 40μm presented an overall better performance. A Python Script to extract key noise performance parameters was also displayed.

Keywords: Microelectromechanical systems (MEMS), Inertial Sensors, MEMS Coriolis Vibrating Gyroscopes, Gyroscopes, Testing, Characterization, Python.

Resumo

Giroscópios MEMS são micro sensores inerciais que conseguem medir o ângulo de orientação ou a variação ângular de uma rotação. Estes dispositivos têm o potencial de ser usados em aplicações de alta precisão para sistemas de navegação, segurança e para eletrónica comercial.

Devido à sua complexidade, os Giroscópios MEMS são propensos a imperfeições que inibem o seu potencial máximo. Através da caracterização extensa destes sensores, é possível validar as metodologias de fabricação, aplicar circuitos de controlo e projetar estruturas mecânicas alternativas que melhorem a sua performance.

Neste projeto é apresentada uma metodologia substanciada para testar e caracterizar estes dispositivos. Os resultados obtidos foram analisados. Adicionalmente, foi desenhado um protótipo de um circuito que opera os sensores em circuito fechado.

Duas famílias de giroscópios com diferentes espessuras foram caracterizadas - 40μm e 100μm. Os dispositivos apresentaram baixos graus de sensibilidade devido a uma forte influência do erro de quadratura. Foi aplicada uma demodulação sensível à fase para melhoramento da performance. Um programa em Python para extrair parâmetros de ruído na resposta é apresentado.

Palavras-chave: Microssistemas eletromecânicos (MEMS), Sensores Inerciais, Giroscópios Vibratórios de Coriolis MEMS, Giroscópios, Teste, Caracterização, Python.

Contents

List of Figures

List of Tables

Acronyms

1DoF One Degrees-of-Freedom 21
2DoF Two Degrees-of-Freedom 3

AC Alternating Current 8
ARW Angle Random Walk 27, 28, 57
ASIC Application Specific Integrated Circuit 4, 11, 13, 15, 34
AV Allan Variance 27, 57

CMOS Complementary-Metal-Oxide-Semiconductor 4, 13
CVG Coriolis Vibratory Gyroscope xv, 3, 4, 6, 9, 10, 17, 31

DC Direct Current 8, 18, 19
DRIE Deep Reactive Ion Etching 11

FFT Fast Fourier Transform 32
FOG Fiber Optic Gyroscope 3

IC Integrated Circuit 13, 15
IEEE Institute of Electrical and Electronics Engineers 9, 17, 25, 27

LCC Leadless Chip Carrier 15, 34
LPF Low Pass Filter 30

MEMS Micro Electro-Mechanical Systems xv, 1, 3, 4, 9, 10, 11, 13, 17, 18, 19, 20, 25, 28, 29, 34, 57
MNS Micro and Nano Systems 13, 15, 18, 19, 21, 25, 32, 34

PCB Printed Circuit Board 1, 11, 15, 32

Q Quality Factor 7, 14

RLG Ring Laser Gyroscope 3
RRW Rate Random Walk 27, 28, 29, 57

SNR Signal to Noise Ratio 4
SoC System-on-Chip 13

ZRO Zero Rate Offset 25, 29

Symbols

A_d	Amplitude of the Driving Force signal 6, 7
A_q	Amplitude of the Quadrature Error signal 8
A_{sense}	Amplitude of the Sensing signal 8
C	Capacitance 53
c_x	Damping coefficient of the x-axis 5
c_y	Damping coefficient of the y-axis 5
F_{drive}	Driving force - a sinusoidal force applied to the actuation electrodes on the driving axis. Same as F_x. 5, 6
F_x	Driving force - force applied in the x-axis 5
F_y	Sensing Force - Force applied in the y-axis, usually employed in a closed-loop mechanism using the actuation/feedback electrodes. 5, 7, 8
G	Gain 15
k_x	Spring constant of the x-axis xv, 5, 6, 7, 8
k_y	Spring constant of the y-axis xv, 5, 7, 8
m	Effective mass (kg) 5, 6
m_x	Effective mass of the x-axis (kg) 5, 7
m_y	Effective mass of the y-axis (kg) 5, 7
Ω_z	Rotation rate on the 0xy plane 5
Q	Charge 53
Q_y	Quality factor of the y-axis oscillator 7

t	Time (seconds) 5
τ_{sense}	Amplitude-decay Time Constant 7
V	Voltage 14, 53
w_x	Resonant frequency of the x-axis oscillator 6, 8, 17
w_y	Resonant frequency of the y-axis oscillator 7, 8, 17
$\dot{x}$	First derivative of x in respect to time - velocity in the x-axis 5
$\dot{y}$	First derivative of y in respect to time - velocity in the y-axis 5

Chapter

1 Motivation and Objectives

MEMS Gyroscopes are complex inertial sensors capable of sensing rotation due to the Coriolis Effect. These devices have the potential to provide reliable and high-performance angular-rate measurements, opening the doors for cheap solutions for navigation and guidance systems, safety systems, and consumer electronics [1]. However, these devices require orders of magnitude of improvement in performance and stability to be used in navigation and tactical applications [2].

Even though matured microfabrication processes have allowed great leaps in the MEMS field, it is known that these devices are prone to have mismatching characteristics to the modelled counterparts [3]. During this study, it will be possible to examine that key parameters from devices of the same batch show divergences between them.

Additionally, the usage of control mechanisms and other strategies to improve the performance requires that the devices are profoundly characterized and their parameters extracted to calibrate them [4]. It is fundamental to streamline the testing and automate it to reduce the time and inconsistencies from fabrication to deployment.

Therefore, the first step to validate and fulfil these enhancements is to extract their performance metrics and compare them with the existing solutions and future iterations.

In order to achieve the objectives of the project, and to improve upon the existing procedures inside the research group, the following tasks were performed:

- Provide a clear methodology for the testing of these devices while at the same time discussing the implications of the results obtained;
- A prototype circuit for MEMS Inertial Sensors was elaborated and the impacts of Printed Circuit Board (PCB) layout design choices were discussed briefly;
- A Python script to extract Noise Performance parameters was developed using existing libraries and adapting it to the available equipment.
- Strategies to identify and mitigate major deteriorating factors like the quadrature error are discussed and exhibited.

Chapter

2 Introduction

A Gyroscope is an inertial sensor that measures the angular rate of rotation or the angle of deflection concerning its frame of reference [5]. The operating physical principle and technology dictate what is the gyroscope type. These can include mechanical gyroscopes (reserved for high cost applications, due to low volume production), optical gyroscopes - like the Ring Laser Gyroscope (RLG) and the Fiber Optic Gyroscope (FOG), and MEMS Gyroscopes [6].

MEMS Gyroscopes have been growing as a research focus due to the low cost and high-performance potential. One of the most common types of MEMS Gyroscope is the CVG, which consists of a suspended vibrating structure which allows motion along the X and Y axes. This Two Degrees-of-Freedom (2DoF) structure is used to extract the angular rotation applied [1, 3]. The devices explored throughout this thesis will be CVG. The principle of operation will be further explained in section 2.2.

2.1 MEMS Gyroscopes

A Microelectromechanical System combines electrical and mechanical structures at a micro-scale through microfabrication technology. The usage of techniques from the semiconductor industry, like photo-lithography, enables creating complex microsystems in bulk, and therefore at a lower cost than alternative technologies [1]. Masses, actuators, springs, and detectors - some of the functional building blocks of these devices, are combined to create systems that respond to external physical stimuli, enabling sensing applications [3].

The obstacles to the widespread use of MEMS Gyroscopes in high precision applications result from the inaccuracy of the angular velocity reading due to many non-trivial factors. The circuit that reads and processes the output may introduce enough noise to hide the sensing response [3]. The inherent variance in the microfabrication processes and the dynamic changes in the environment conditions, like temperature, considerably affect the sensor's performance [7]. In the mechanical spectrum, solutions to overcome these obstacles have been put by redesigning the MEMS structure to diminish unwanted excitations [8–10]. Research efforts are also placed into the electrical domain, by creating digital control mechanisms of the MEMS mechanical parts [11], reducing noise in the

readout circuit [12] and novel mixed-signal processing techniques to increase the Signal to Noise Ratio (SNR) [13].

The integration of the sensors with Application Specific Integrated Circuit (ASIC) using Complementary-Metal-Oxide-Semiconductor (CMOS) technology is so prevalent and impactful that the performance of the gyroscope becomes highly dependent on it. The capability to integrate the control and signal processing electronics in the same die as the sensor is another advantage of MEMS based sensors, justifying the research efforts put into this technology [14].

2.2 Theoretical Working Principle

The model of a conventional CVG gyroscope can be seen in figure 2.1. The model is based on a proof-mass attached with elastic springs to a frame, such that it is capable of oscillation in the x and y-direction. These two orthogonal modes of vibration are the drive-mode or primary mode and sense-mode or secondary mode. Depending on the actuation and detection design schemes, these vibrating modes can be interchangeable.

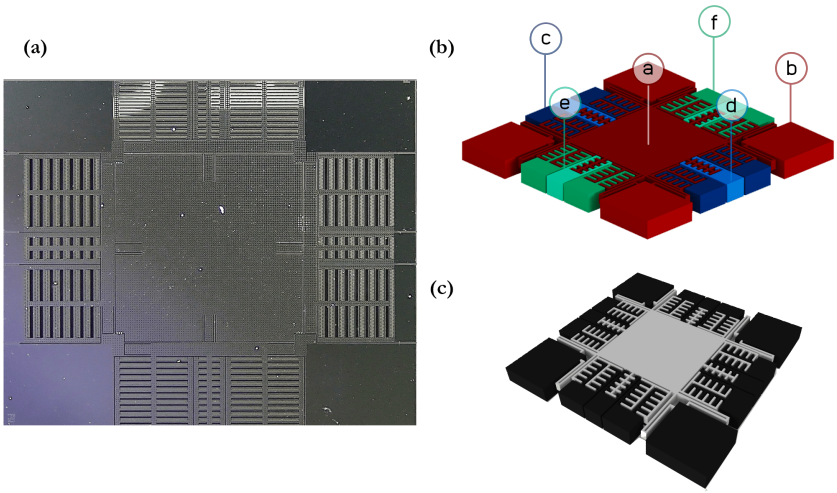

Figure 2.1: **Conventional Vibratory Gyroscope (a)** An Optical Microscope image of a CVG. **(b)** Simplified model of the CVG: a - suspended proof mass; b - elastic springs attached to anchors; c/d - driving-mode actuation and detection comb fingers; e/f - sensing-mode actuation and detection comb fingers. **(c)** Simplified model of the CVG: in grey are represented the suspended movable parts of the gyroscope, constrasting with the anchored parts in black.

The dynamics of operation are derived from concepts of classical mechanics. A planar, z-axis vibratory gyroscope is considered, based on the Coriolis effect, whose principle dictates that a moving object tends to continue vibrating in the same plane even if its supporting frame rotates [15]. MEMS Capacitive Coriolis Vibratory Gyroscopes take advantage of this phenomena by having one of the oscillatory modes driven into resonance, much like a pendulum in a swinging motion [16].

The mass is forced to vibrate along the x-axis (drive-mode). The folded support

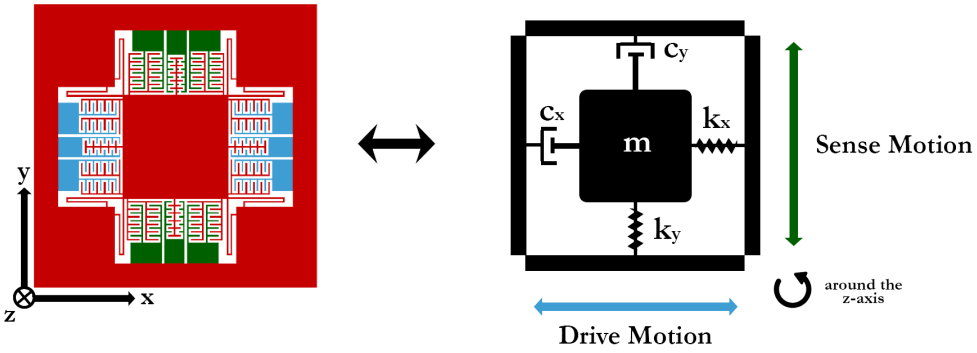

Figure 2.2: Lump model illustration of a CVG - the proof mass is free to oscillate in two principle orthogonal directions: drive and sense. Adapted from [3].

beams isolate the motion of each axis, separating the driving-mode from the sensing-mode. When the sensor suffers a rotation, a displacement is generated in the y-axis. Both modes can be considered as a "spring-mass-damping" second-order vibrating system (see figure 2.2) [17].

The motion equation of a vibratory gyroscope can be taken through the second time derivative of the position vector - thus expressing the acceleration experienced by a body on a rotating frame. The following equations were based on Acar *et al.* [3] and Trusov [2] solutions for the motion dynamics of these devices.

Assuming that the coupling between the two modes is zero, the drive-mode axis is x, and the sense-mode axis is y, the equations that describe the dynamics of the system are:

$$F_x + 2m_y\Omega_z\frac{\delta y}{\delta t} = m_x\frac{\delta^2 x}{\delta t^2} + c_x\frac{\delta x}{\delta t} + k_x x \tag{2.1}$$

$$F_y - 2m_x\Omega_z\frac{\delta x}{\delta t} = m_y\frac{\delta^2 y}{\delta t^2} + c_y\frac{\delta y}{\delta t} + k_y y \tag{2.2}$$

Where F_x is the force applied to the drive mode, F_y is the force applied in the sense mode, m_x / m_y are the effective masses, c_x / c_y are the damping coefficients, and k_x / k_y are the spring constants. $2m_y\ \Omega_z\ \dot{y}(t)$ and $-2m_x\ \Omega_z\ \dot{x}(t)$ are the Coriolis forces coupling the two modes. The term Ω_z is the applied rotation rate in the xy plane.

Since F_x is the electrostatic force applied by the driving comb fingers, it will be denominated as F_{drive}. Furthermore, the conventional gyroscope presented has only one mass, resulting in $m = m_x = m_y$. Since the sense mode Coriolis response is orders of magnitude inferior to the driving force, the term $2m\Omega_z\dot{y}$ in equation 2.1 becomes negligible aswell [18]. Thus:

$$F_{drive} = m\frac{\delta^2 x}{\delta t^2} + c_x\frac{\delta x}{\delta t} + k_x x \tag{2.3}$$

$$F_y - 2m_x\Omega_z\frac{\delta x}{\delta t} = m\frac{\delta^2 y}{\delta t^2} + c_y\frac{\delta y}{\delta t} + k_y y \tag{2.4}$$

The applied F_{drive} is usually a periodic signal in the form of:

$$F_{drive} = A_d sin(w_x t) \tag{2.5}$$

$$w_x = \frac{k_x}{m} \tag{2.6}$$

Where A_d is the driving amplitude, and w_x is the resonant frequency of the proof mass. The term w_x can be obtained by dividing the stiffness (k_x) of the proof mass on the x-direction by its mass (m).

There are two modes of operation of CVG gyroscopes: open loop and closed loop. The impacts of both on the motion dynamics of the device will be discussed in section 2.2.1.

2.2.1 Open Loop vs Closed Loop operation

The conventional mode of operation is classified as open-loop mode, whereas when a feedback circuit is applied to control the proof mass dynamics, it is considered closed-loop [2]. For both modes, the underlying principle of operation is similar - the excitation of an oscillation in the sense-mode via the Coriolis effect [19].

In both modes, operation starts by driving the gyroscope into resonance. The displacement of the proof mass (drive position in figure 2.3) occurs in the form of:

$$x = A_d cos(w_x t) \tag{2.7}$$

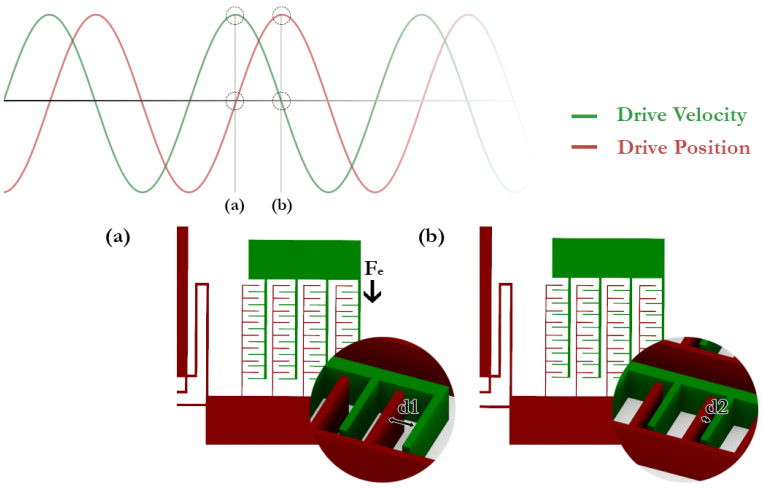

Figure 2.3: Drive dynamics illustration. The drive position (red) and drive velocity (green) caused by the electrostatic force $F_{drive} = A_d sin(w_x t)$. (a) Rest position of the proof mass; (b) Maximum displacement of the proof mass.

In an open-loop operation, the equation 2.4 can be taken and F_y nulled, since no force is applied in an open-loop control scheme:

$$-2m_x\Omega_z\frac{\delta x}{\delta t} = m\frac{\delta^2 y}{\delta t^2} + c_y\frac{\delta y}{\delta t} + k_y y \tag{2.8}$$

This equation has a solution in the form of [20]:

$$y = -A_d\tau_{sense}\Omega_z cos(w_x t) \tag{2.9}$$

In the equation above, A_d is the driving amplitude, $\Omega_z cos(w_x t)$ the modulation induced by the Coriolis effect, and τ_{sense} is the amplitude-decay time constant, which results from:

$$\tau_{sense} = \frac{2Q_y}{w_y} \tag{2.10}$$

Here, $w_y = \sqrt{\frac{k_y}{m}}$ is the natural frequency of the secondary-mode. Q_y is the Quality Factor (Q), which is a merit-figure of any resonator given by:

$$Q_y = \frac{w_y m}{c_y} \tag{2.11}$$

The difference between open-loop and closed-loop lies in the controlled displacement of the sense axis. When operating in a closed-loop mode, the proof mass is re-balanced through a control circuit in order to stay at $y = 0$ by applying a force F_y in the form of:

$$F_y = A_{sense} sin(wt) \tag{2.12}$$

The principle behind it being that if y is kept at a resting position, it implies that:

$$F_y - 2m_x\Omega_z\frac{\delta x}{\delta t} = 0 <=> F_y = 2m_x\Omega_z\frac{\delta x}{\delta t} \tag{2.13}$$

Being $2m_x\Omega_z\dot{x}(t)$ the Coriolis response, in which the rate of rotation of the sensor can be extracted indirectly by the applied F_y.

In terms of impact, operating in open loop translates to a smaller scale factor stability, dynamic range, and linearity – resulting in an overall worse performance. In spite of this, it requires a less complicated circuit than its counterpart [21].

2.2.2 Impacts of the Quadrature Error on Gyroscope Performance

In micromachined vibratory gyroscopes, fabrication imperfections introduce small imbalances in the gyroscope mechanical parts, resulting in interference between the modes [22]. The imbalance resulting from non-balanced suspension beams and proof mass ($m_x \neq m_y, k_x \neq k_y$) results in a non-zero output when the gyroscope has no mechanical input – called the Quadrature Error – that can obfuscate the Coriolis motion [23]. This error source is proportional to the drive-mode position, since it originates from the

spillover of the drive-mode dynamics on the sense-axis. It differs from the Coriolis signal, which is proportional to the drive-mode velocity, resulting in a 90º phase difference ($\phi_{Coriolis} = \phi_{Quadrature} - 90°$) for a mode-matched gyroscope ($w_x = w_y$) [3].

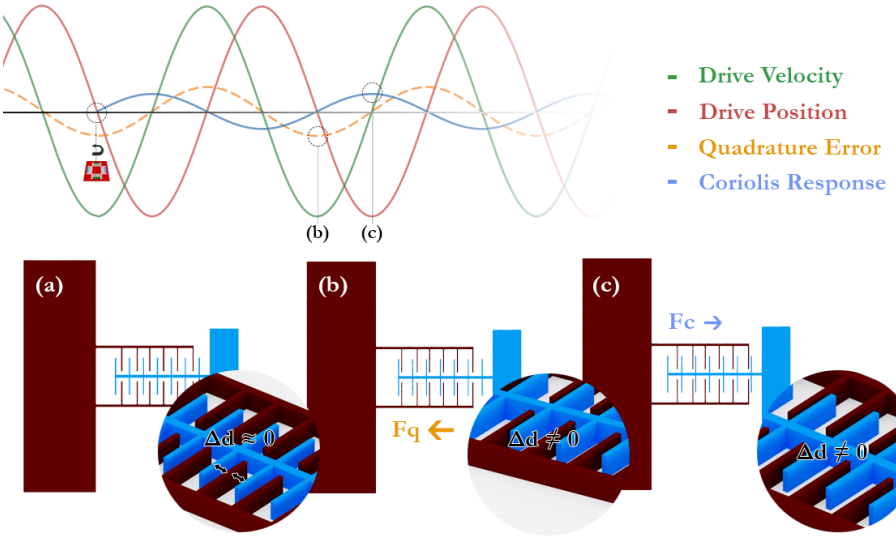

Figure 2.4: Illustration on the effect of the quadrature error. The drive position, drive velocity, Coriolis response and quadrature phase relations for mode-matched system where $k_x \neq k_y$. (a) ideal case, with quadrature force cancellation ($F_q = 0$); (b) non-zero output for a zero Coriolis input; (c) pure Coriolis response.

A combination of solutions to suppress the Quadrature Error have been researched: trimming (using laser or focused ion beam) to resolve the non-orthogonality of the mechanical structures, which are expensive and time-consuming answers [23]. Alternatively, suppressing the quadrature error using additional mechanical levers has been tried [24] or by applying a Direct Current (DC) signal to actuating comb fingers, translating in electrostatic forces that act as additional levers, making $k_x = k_y$ [25].

An Alternating Current (AC) signal could also be applied to the secondary-mode in a closed-loop operation, with the requirement that the phase and the amplitude of the sense output are matched.

In this case, F_y would be:

$$F_y = A_{sense} sin(wt) + A_q cos(wt) \tag{2.14}$$

Where the first term $A_{sense} sin(wt)$ nulls the Coriolis force, and $A_q cos(wt)$ cancels the quadrature error [20].

Moreover, the inherent phase difference between the two signals (see figure 2.4) allows phase-sensitive demodulation techniques to isolate the gyroscope's real output, yet needing a more complex readout circuit [26].

2.3 Performance Metrics

In terms of the most important features used to describe and quantify the characteristics of CVG, there is an emphasis on two major characteristics:

The Scale Factor, which is the rate of transfer between the input and output signals in the linear regime of measurements, and it is highly related to the sensitivity of the device. Common sources of error in MEMS Gyroscopes are the fabrication imperfections, floats on the resonance frequencies and quality factors, and other unwanted excitations [2, 3].

The Bias, or Zero Rate Offset, which is the apparent output of the sensor when no input rate is being applied, usually expressed in degrees per time unit. One of the major sources of Bias is the quadrature error, discussed previously in 2.2.2 [2].

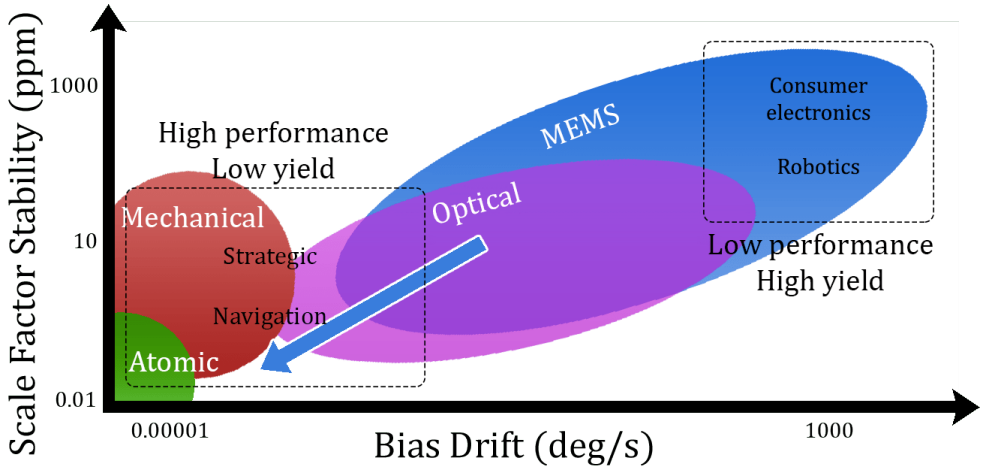

Figure 2.5: Scale factor stability, expressed in parts per million (ppm), as a function of the bias stability, dependent on the gyroscope technology type. Adapted from [6].

The performance of gyroscopes is usually divided into three categories: rate, tactical and inertial. In table 2.1, some of the breaking points of each characteristic are shown.

Table 2.1: Performance requirements for each gyroscope grade [2]

Parameter (unit)	Rate	Tactical	Inertial
Angle Random Walk (deg/$\sqrt{h}$)	>0.5	0.5-0.05	<0.001
Bias Stability (deg/h)	10-1000	30-1	<0.06
Scale Factor Stability (ppm)	100-1000	10-100	<1
Linearity Range (deg/s)	50-1000	>500	>400
Bandwidth (Hz)	>70	100	100

To consult every performance characteristic, refer to the Institute of Electrical and Electronics Engineers (IEEE) Standard Specification Format Guide and Test Procedure for Coriolis Vibratory Gyros [40]. In order to improve the grade of MEMS CVG, breakthroughs in terms of design features, control circuits, data post-processing, and others strategies are currently being researched.

2.3.1 Dual-mass MEMS Gyroscopes enhancements

By employing a double-mass design, the MEMS Gyroscopes are reported to be less sensitive to ambient fluctuations, and unwanted vibrations [27, 28], using a 2-DOF sense mode structure would improve the robustness of the sensor due to the common mode rejection capability [3].

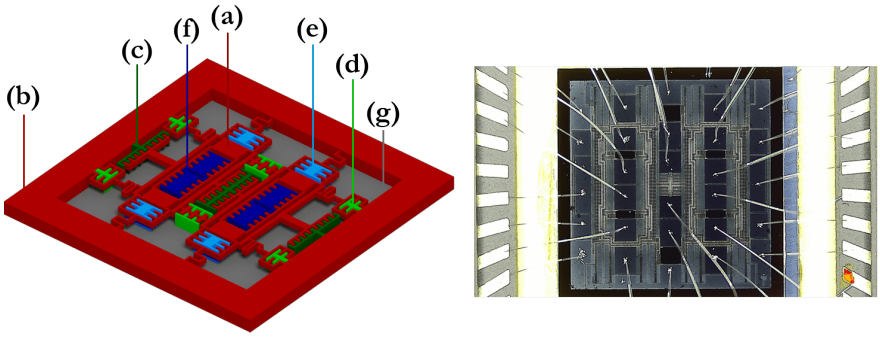

Figure 2.6: Simplified schematic and optical microscope picture of the dual-mass MEMS CVG studied in this project. (a) Suspended proof mass (b) Supporting frame, anchored to the substrate (c) Driving actuation comb fingers (d) Drive detection comb fingers (e) Sense detection comb fingers (f) Sense actuation comb fingers (g) Substrate

The operation principle of these gyroscopes remains unchanged from the conventional ones. The difference lies in both masses being driven anti-phase in relation to each other, meaning that the Coriolis response in the sense-mode will occur with an anti-phase displacement as well.

This results in a fully differential sense signal (between the two masses), which will preserve the angular rate signal and reject external excitations other than the Coriolis force. Furthermore, due to the use of the two masses, the scale factor should double [3].

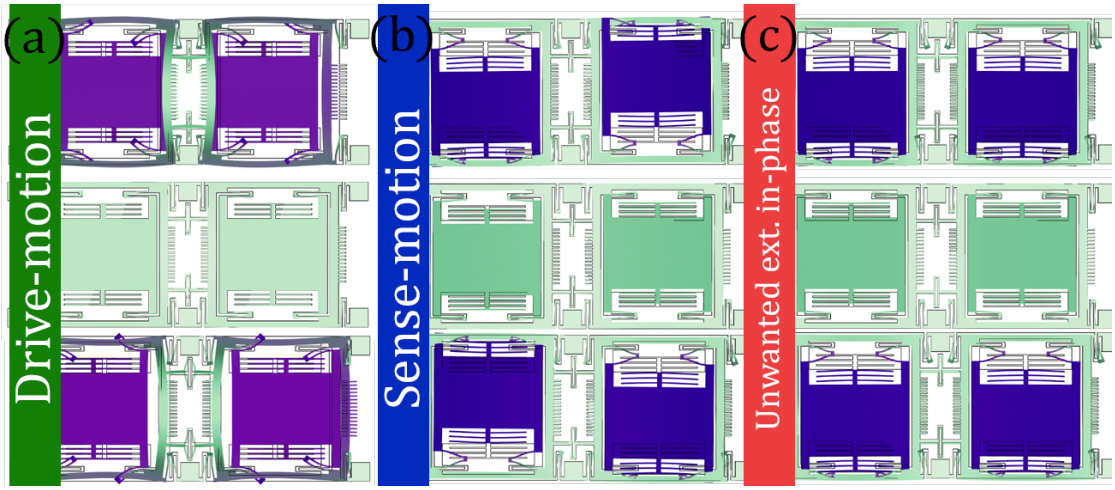

Figure 2.7: Comsol simulations of the dynamics of a double-mass anti-phase gyroscope: (a) Anti-phase drive mode motion (b) Anti-phase sense mode motion (c) In-phase unwanted excitations due to external shocks. The simulated gyroscope is based on [3].

Chapter

3 Materials and Methods

The eight sensors used throughout this project were previously fabricated using Deep Reactive Ion Etching (DRIE) on 40μm and 100μm Poly-Si wafers. Since the design and fabrication of these devices is beyond this project's scope, they will not be discussed in this study. After the fabrication, an external company packaged the devices.

The PCB layouts were designed using Altium Designer through a student license. Altium Designer is a PCB and electronic design software for printed circuit boards, and it is the industry standard in this field. It was utilized to prototype the Inertial Sensor Board, to be integrated with an external ASIC.

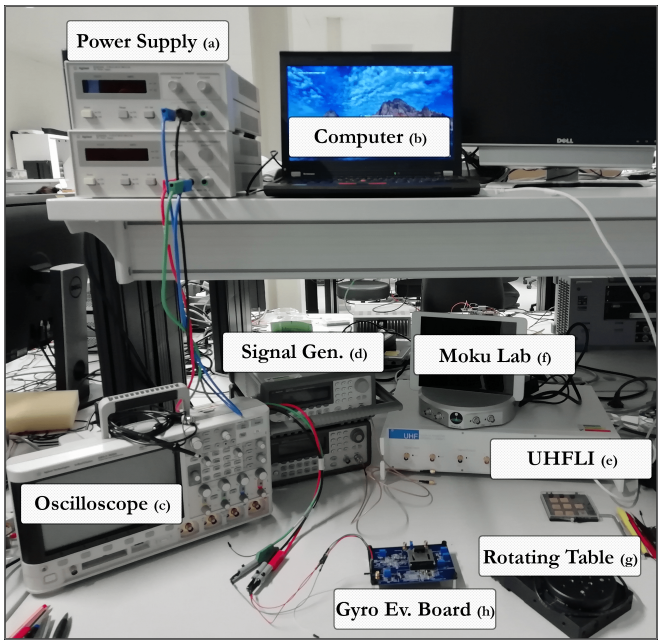

Figure 3.1: Equipment used throughout the project

In order to characterize the MEMS Gyroscopes, the following equipment was utilized:

- (a) - Two Agilent E3610A DC Power Supplies – capable of feeding 0-15V, 0-2A. They were used primarily to feed the PCB readout circuits;

- (b) - A computer to process the data and utilize the apps related to the Zurich Instruments UHF Lock-In Amplifier;
- (c) - An Agilent Technologies DSO-X 3034A (350 MHz – 4GSa/s) Oscilloscope – to read, examine, transform and capture the data utilized throughout this project;
- (d) - Two Agilent 33250A 80Mhz Function/Arbitrary Waveform Generators – to inject the signals related to the Carrier wave and driving of the MEMS Gyroscopes;
- (e) - The Zurich Instruments UHF Lock-In Amplifier is a digital instrument that covers the frequency range from DC to 600 MHz and allows the characterization of MEMS devices. It was used for the frequency and phase sweeping, and other noise measurements.
- (f) - The Moku Lab is a digital multi-function instrument that was used as a Lock-In Amplifier to demodulate the Quadrature Error.
- (g) - A Thor's Labs Rate Rotating Table – to characterize the rotation response of the MEMS Gyroscopes.
- (h) - MNS Gyro Evaluation Board – a printed circuit board which will be discussed in Section 4, used to extract the signal out of the devices.

The detailed use of the equipment will be discussed in-depth in Section 5.

Furthermore, the programming language Python was utilized to automatize the noise measurements processes related to the Allan Variance. Due to being a high-level language suited for scientific and engineering environments, various libraries are developed as open-source projects such as the ones utilized in this project [29]. This study makes use of Pandas [30], which is an open source data analysis and manipulation tool, NumPy [31] to enable numerical computing, and AllanTools [32] to calculate the coefficients needed to extract the values of the Allan Variance.

Chapter

4 Circuit Design

Having a physical device that responds to external stimuli is not a sensor in itself. The mechanical parts are usually integrated with a circuit to output a readable response [33].

Progress in physics, chemistry, material science and electronics related to fabrication technologies have allowed the integration of low-cost, miniaturized System-on-Chip (SoC) for many applications [34]. Furthermore, the same materials (silicon, poly-silicon, metals, dielectrics, metal-oxides, and others) and processes are used to fabricate both the sensors and the integrated circuits in CMOS technology. These advances have opened new opportunities for research on electronic interfaces [35].

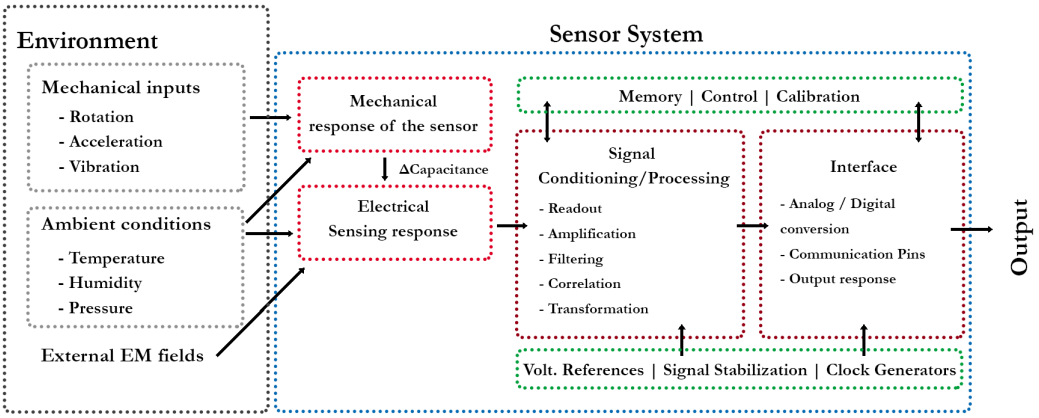

Figure 4.1: Example of a gyroscope sensor hierarchy. Adapted from [33].

Although this SoC integration is desirable in terms of performance, a generalized solution to test these sensors is needed not to waste Integrated Circuit (IC)s or MEMS when one of them is subpar or non-functional. In that way, the research group Micro and Nano Systems (MNS) at KU Leuven developed a fully analogue Gyroscope Evaluation Board that operates in open-loop exclusively. This circuit is going to be analyzed in section 4.1.

A prototype circuit capable of operating in a closed-loop was designed to overcome the conventional mode of operation's shortcomings. For this purpose, an ASIC for inertial

sensors was integrated with the devices. This circuit will be explored in section 4.2.

4.1 MNS Gyro Evaluation Board

The readout circuit's primary function is to convert the charge (Q) change due to the comb fingers' displacement into a voltage (V). For additional information regarding the capacitive electrodes, refer to Annex D. The rest of the circuit can then interpret this voltage. The topology of this circuit is based on amplitude demodulation, where the change in capacitance is converted to a change in the voltage amplitude of the output signal.

The change in capacitance in the variable capacitors of the sensing-mode axis is measured by an interface based on differential charge amplifying. By connecting two parallel charge amplifiers on each electrode, the outputs at the top and bottom electrodes function independently and are subtracted from each other to give a final measurement. This circuit is based on the same working principle as Almutairi, B. [36] for MEMS accelerometers.

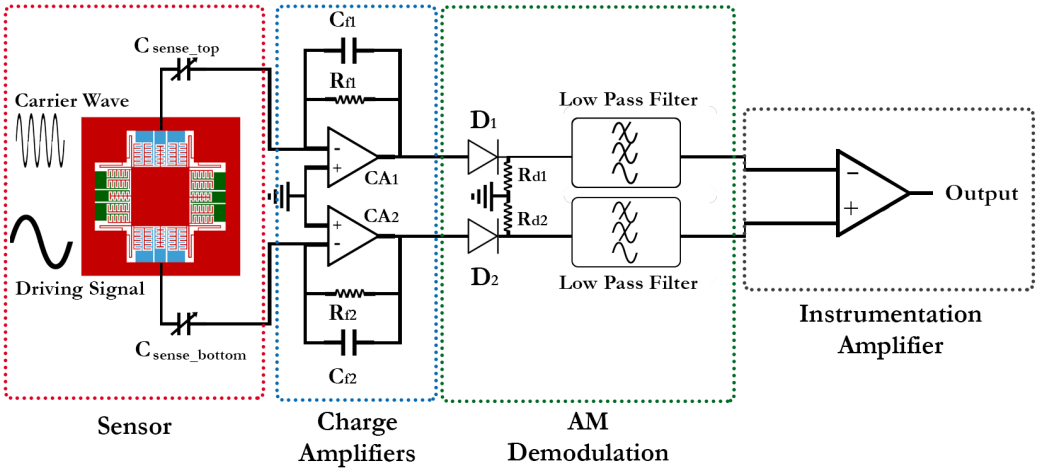

Figure 4.2: Readout circuit simplified schematic.

The sensing element can be considered a variable capacitor, connected to a voltage source with the carrier signal. One of the sense electrodes is connected to the virtual ground input of the charge integrator [36].

A charge amplifier is a particular class of circuits that have typically low bias currents. These amplifiers are employed to convert to voltage signals from capacitive sensors, which generate minimal charges (on the order of pico coulombs) [37]. A basic circuit of a charge-to-voltage converter is shown in figure 4.2. The transfer function of the charge integrator is:

$$V_{out} = -\frac{\Delta Q}{C} \tag{4.1}$$

In order to extract the response signal from the carrier wave, an amplitude demodulation is employed using a simple diode rectifier followed by a low pass filter. The diode outputs the halved enveloped signal. This output goes through the low pass filter, where the high-frequency signal coming from the carrier wave is rejected.

The function of the Instrumentation Amplifier is to amplify and differentiate the output signal, which is proportional to the difference in voltages between its two inputs:

$$V_{out} = G(V_{top} - V_{bottom}) = G\Delta V \tag{4.2}$$

Where G is the finite gain of the device, and V_{top}/V_{bottom} the output of the low pass filters.

4.2 Inertial Sensor Board Prototype (ISB)

A prototype was developed during this project in order to operate the gyroscopes under a closed-loop. For this effect, it was utilized the ASIC SW1121. The chip acts as an interface for the gyroscope sensing element. It consists of a drive loop connected to the drive electrodes, and a sense path connected to the sense electrodes. It also includes all the digital processing needed to extract and output the Coriolis signal. The in-depth functioning of the IC is beyond the scope of this work. On the other hand, the PCB layout is an essential step of the sensor circuit design, which can be briefly discussed.

4.2.1 Bonding Mechanism

The bonding scheme will define how the sensor will interface with the circuit. Since the pin requirements vary from sensor to sensor, the designers' job is to determine what type and how the bonding will proceed. At MNS, wire bonding [38] is usually employed to connect the silicon from the PCB to the pads from where the charge will be extracted. The two most common bonding packages are Leadless Chip Carrier (LCC) (LCC - 48 pins) and PCB carriers (24 pins), which can be seen in figure 4.3.

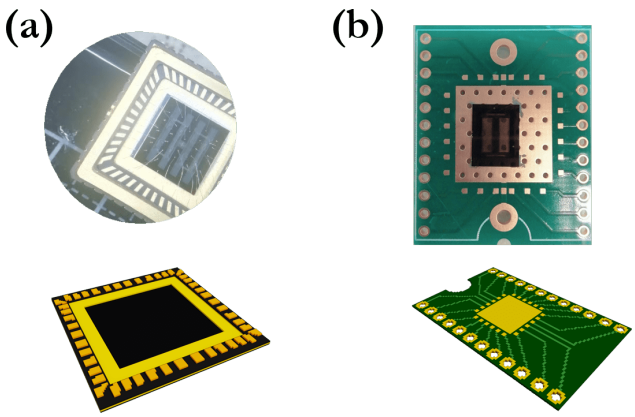

Figure 4.3: Examples of carriers used in this project (a) LCC48 with a bonded MEMS Gyroscope; (b) PCB carrier with an unbounded accelerometer.

4.2.2 Trace Length and Matching

Sensors require, as a rule of thumb, traces that are as short as possible (to minimize interference and loss of signal) while also being equivalent in length when employing differential signals (which is the case of inertial sensors) [35].

The most important connections are the sensing pins, so when choosing the bonding scheme, it is crucial to consider the synergy between those and the circuit.

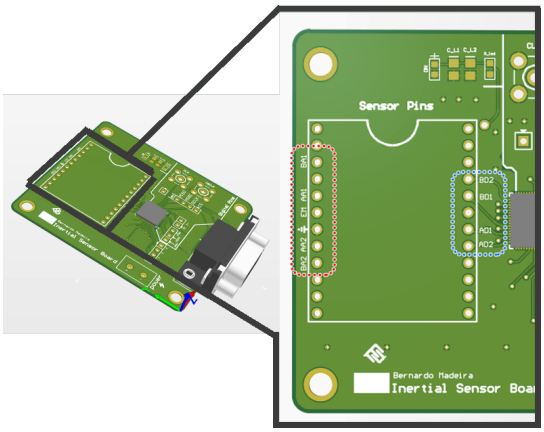

Figure 4.4: Inertial Sensor Board - sensing pins illustration. In blue are the pins related to the sensing loop, which are prioritized to be as short as possible. The red box indicates the actuation and power related pins.

Since the gyroscope sensing signal is a differential signal, it is important that the traces for both signals have the same length so that the propagation delay times are equal [39]. This can be realized by making one of the signal traces go through a longer path like exemplified in figure 4.5.

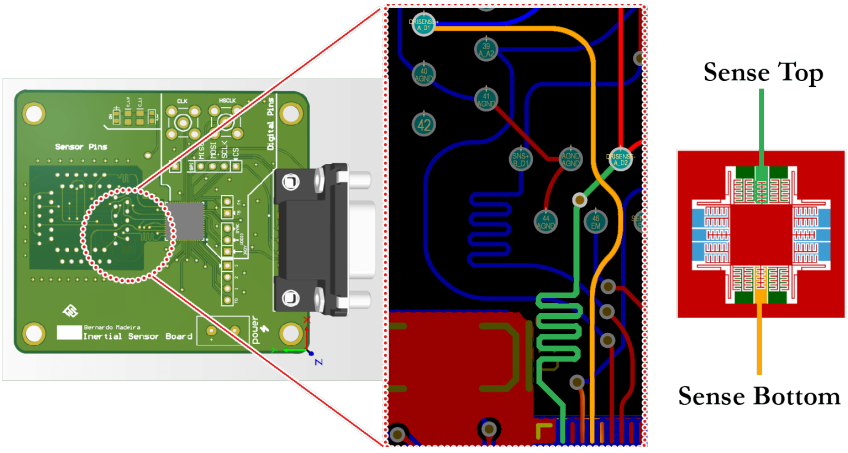

Figure 4.5: Illustration of length tuning in the Inertial Sensor Board. Since the pad for the top sense (green) is closer, the trace is designed to go a longer path, matching the length that the bottom sense signal (orange) has to travel.

Chapter

5 Results and Discussion

The characterization procedure followed the standards outlined in the IEEE Standard Specification Format Guide and Test Procedure for Coriolis Vibratory Gyros [40].

The tested devices are dual mass, and frequency mismatched Capacitive CVG. To improve the stability and linearity of the MEMS Gyroscopes, both resonance modes are slightly mismatched ($w_x \neq w_y$) [41]. Although in Section 2.2 a conventional gyroscope was presented to simplify the theoretical explanations, the tested devices are slightly more complex in terms of design and functioning. Even though this is the case, the working principle logic remains unchanged.

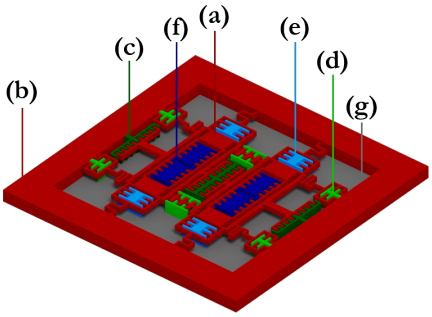

Figure 5.1: Dual Mass Coriolis Vibratory MEMS Gyroscope - (a) Proof mass with springs attached to the frame; (b) Frame; (c) Drive actuation electrodes; (d) Drive detection electrodes; (e) Sensing detection electrodes; (f) Sensing actuation electrodes; (g) Substrate

5.1 Rate Transfer Tests

The rate transfer expresses the relationship between the change in the actual input rate and the sensor output as a controlled excitation is applied on each mode. This procedure can be realized using the actuation electrodes to induce a displacement on the vibrating mode and measuring it. To determine the scale factor - the transfer rate from the driving mode to the sensing mode due to the Coriolis Effect - a rotating table is used, and a known rotation rate is applied in order to measure the output [42]. Only the first method was utilized.

5.1.1 Driving Mode

The testing conditions were maintained for every MEMS Gyroscope. The applied carrier wave to the proof mass was $2.002MHz$, the injected driving signal applied in the actuation sense electrodes was a sine wave with amplitude $A = 5V$ and frequency $f = 10kHz$. No DC offset was applied. The used circuit was the MNS Gyro Evaluation Board, which was referenced in section 4.1.

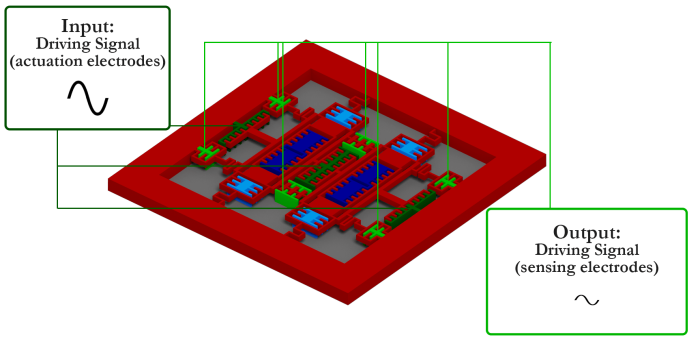

Figure 5.2: Transfer rate test actuation scheme of the driving mode.

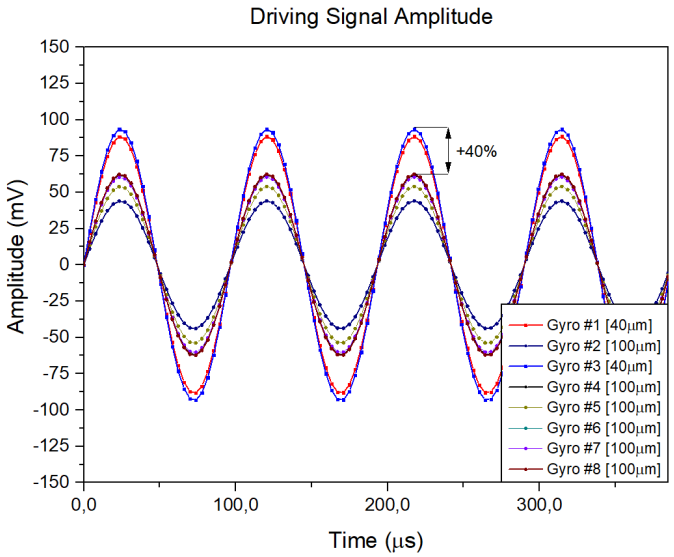

Figure 5.3: Amplitude plot of the driving mode responses.

The recorded amplitude values can be seen in Table 5.1. On average, the 40μm gyroscopes overperformed in terms of rate transfer compared to its thicker counterparts. The best 40μm sensor (Gyroscope #3) response is 40% higher in comparison to the best 100μm devices (Gyroscope #6 and #8). Since the applied electrostatic force is the same for both type of devices, it is expected that the thinner proof masses will experience a higher displacement. The oscilloscope readings can be verified on Appendix A.

Table 5.1: Rate transfer response of the driving mode.

Device	Thickness	Amplitude (mV)
Gyroscope #1	$40\mu m$	177
Gyroscope #2	$100\mu m$	88
Gyroscope #3	$40\mu m$	187
Gyroscope #4	$100\mu m$	124
Gyroscope #5	$100\mu m$	108
Gyroscope #6	$100\mu m$	125
Gyroscope #7	$100\mu m$	121
Gyroscope #8	$100\mu m$	125

5.1.2 Sensing Mode

The testing conditions were maintained for every MEMS Gyroscope. The applied carrier wave to the proof mass was $2.002MHz$, the injected driving signal was applied in the actuation sense electrodes, a sine wave with amplitude $A = 5V$ and frequency $f = 10kHz$. No DC offset was applied. The used circuit was the MNS Gyro Evaluation Board.

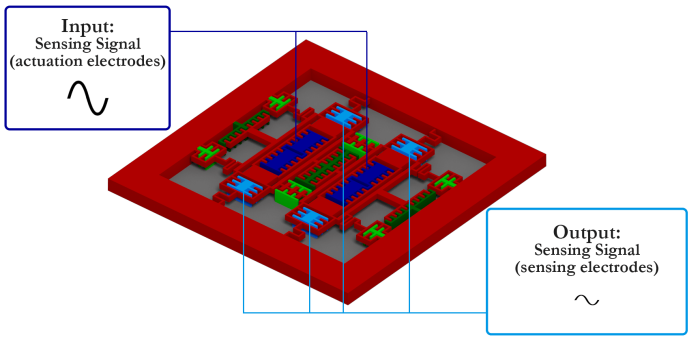

Figure 5.4: Transfer rate test actuation scheme of the sensing mode response.

The recorded amplitude values can be seen in Table 5.2. The 40μm gyroscopes overperformed in terms of rate transfer of the secondary mode compared to the thicker counterparts. There is a notorious gap in transfer rate between both types of devices. Gyroscope #3 has at least a 590% difference to the best 100μm device - Gyroscope #4, which presents a sensing amplitude of 44.6mV. Even between the two best performing sensors, Gyroscope #1 underperforms Gyroscope #3 by 233%. If gyroscope #7 is not considered, the 100μm devices show an average amplitude of $40.2mV$.

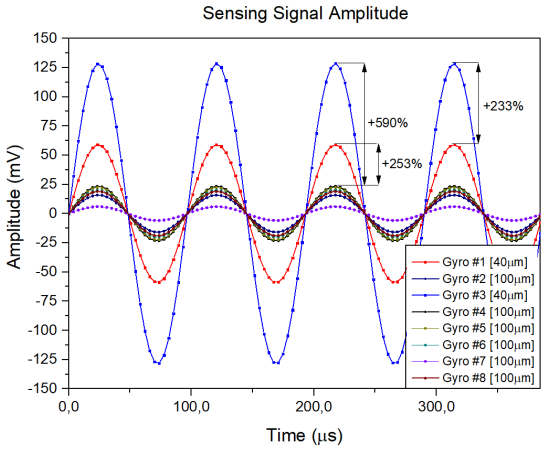

Figure 5.5: Amplitude plot of the sensing mode responses.

Table 5.2: Rate transfer response of the sensing mode of the tested devices

Device	**Thickness**	**Amplitude (mV)**
Gyroscope #1	$40\mu m$	118
Gyroscope #2	$100\mu m$	31.8
Gyroscope #3	$40\mu m$	275
Gyroscope #4	$100\mu m$	46.6
Gyroscope #5	$100\mu m$	44.6
Gyroscope #6	$100\mu m$	40.2
Gyroscope #7	$100\mu m$	11.9
Gyroscope #8	$100\mu m$	38

Given that in normal operation the sensing mode is excited by the Coriolis force, which is given by:

$$F_{Coriolis} = 2m\Omega_z \frac{\delta x}{\delta t} \tag{5.1}$$

It can be seen that having a large proof mass is preferable for increasing sensitivity, since the detection force is proportional to the mass. On the other hand, the presented 100μm devices have considerably worse transfer rates. Since the thickness increase happens to all the suspended parts, not only the mass is bigger, but the stiffness of the beams also increases. This increase in stiffness may result in a bigger influence to the dynamics of the gyroscope than the increase in mass.

The MEMS Gyroscopes built with a thickness of 40μm are therefore better candidates to present a Coriolis response.

The oscilloscope data presented on this subsection can be verified on Appendix A.

5.2 Frequency and Phase Sweeping

An effective measurement of any resonator's dynamical parameters is to experimentally acquire the frequency response by doing a frequency sweep while detecting the capacitive response of the device at the same time.

The test was realized using the MNS Gyro Evaluation Board, connected to the Zurich Instruments UHF Lock-In Amplifier. A sine wave signal with an amplitude voltage of 1.5 V with varying frequency is injected into the actuation electrodes. The output is read using the sensing electrodes response of the same oscillation mode. This means that each vibration mode will be inspected separately in a frequency range near the oscillation peak projected for the devices.

The devices were modelled to have a 10kHz drive mode resonant frequency. The sense mode resonant frequencies were projected to have a slight mismatch. By doing the frequency sweeping, it is possible to infer if the fabrication procedure yielded the expected results.

Table 5.3: Projected values for frequency mismatch between Driving and Sensing Modes

Device	D-Mode Peak (Hz)	S-Mode Peak (Hz)	Δ Frequency (Hz)
Gyro #1 ($40\mu m$)	10000	10134	134
Gyro #2 ($100\mu m$)	10000	10027	27
Gyro #3 ($40\mu m$)	10000	10106	106
Gyro #4 ($100\mu m$)	10000	10032	32
Gyro #5 ($100\mu m$)	10000	10032	32
Gyro #6 ($100\mu m$)	10000	10027	27
Gyro #7 ($100\mu m$)	10000	10019	19
Gyro #8 ($100\mu m$)	10000	10019	19

Since every oscillation mode is being tested like a One Degrees-of-Freedom (1DoF) resonator, the ideal behavior of the gyroscope would follow the model of that ideal system, as it is illustrated in figure 5.6. The peak corresponds to the resonant frequency of the device, which is given by equation 2.6, discussed in Section 2.2. Furthermore, the phase of the device should decrease by 180°, with the 90° phase shift point being coincident to the resonant frequency [43].

5.2.1 Driving Mode

Since the projected resonant peaks are near the $10kHz$ frequency, the frequency sweep was executed from $8kHz$ to $12kHz$. A driving voltage of $1.5V$ was applied in the injected sine wave signal. The test actuation scheme was the same as in section 5.1.1.

The most noticeable feature is the rise of the amplitude value with the increasing frequencies (see figure 5.7). This is a reported occurrence when doing this type of test, and it is attributed to the feed-through current of parasitic interference. Due to the conductive substrate and no use of shielding of the circuit, the current can run over a

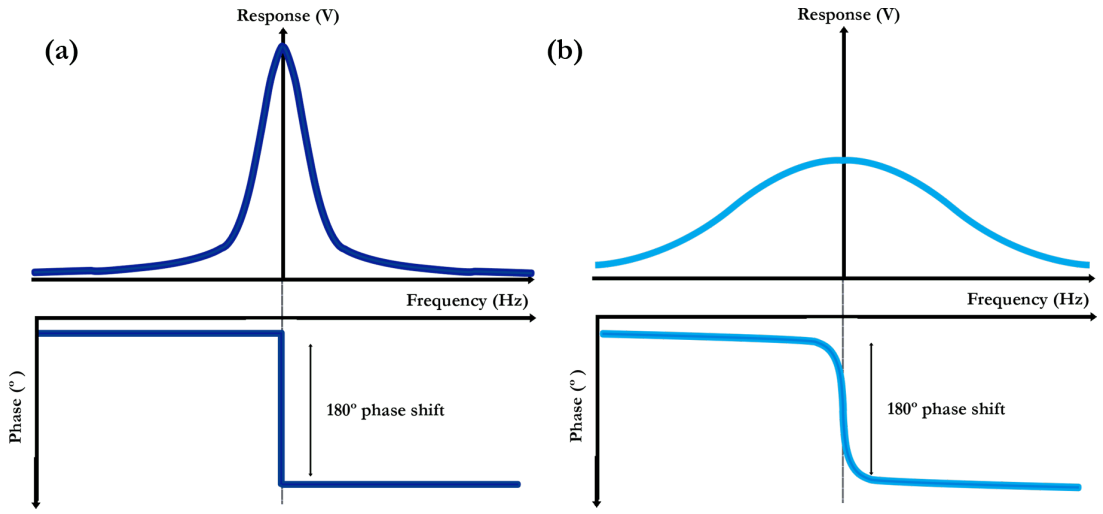

Figure 5.6: Frequency and phase response of a resonator. (a) Model of an ideal resonator. (b) Model of a non-ideal resonator. Due to dissipative forces, the devices present a behavior that follows more closely this model. Adapted from [43].

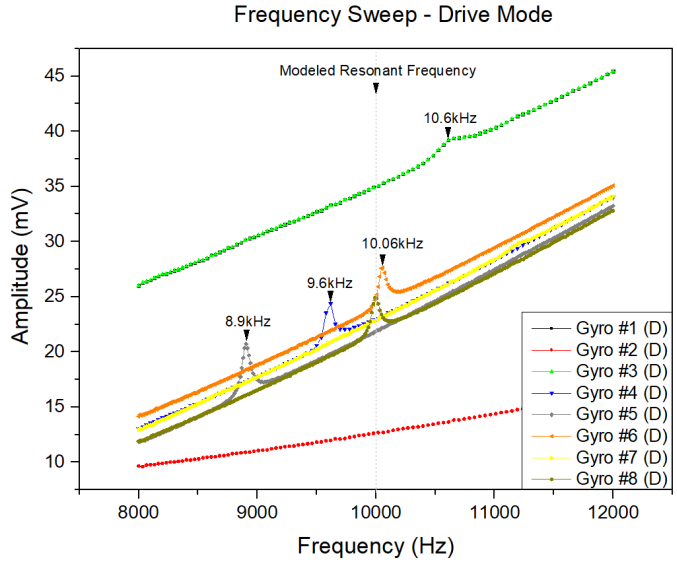

Figure 5.7: Plot of the frequency sweep - driving mode response.

parasitic capacitance between the driving pad, the substrate, and the sensing pad causing the ramping of the measured values [3].

Secondly, it is possible to verify that no resonant peaks were detected for gyroscopes #2 and #7. On the other hand gyroscopes #1 and #3 exhibit almost the same dynamic behavior, with a resonant peak near $10.6kHz$.

The $100\mu m$ devices display similar operation, but their resonant peaks vary much more between them than the $40\mu m$ counterparts. However, they also present the closest real peak values to the projected peaks, as it is possible to see in Table 5.4.

Table 5.4: Frequency response of the driving mode.

Device	Expected Peak (Hz)	Real Peak (Hz)	Δ Frequency (Hz)
Gyro #1 (40μm)	10000	10641	641
Gyro #2 (100μm)	10000	No peak	NaN
Gyro #3 (40μm)	10000	10630	630
Gyro #4 (100μm)	10000	9622	388
Gyro #5 (100μm)	10000	8898	202
Gyro #6 (100μm)	10000	10045	45
Gyro #7 (100μm)	10000	No peak	NaN
Gyro #8 (100μm)	10000	9995	5

5.2.2 Sensing Mode

The projected resonant peaks are near the $10kHz$ frequency even though they were designed with a frequency mismatch - as it is verified in Table 5.3. The frequency sweep for the sensing mode was also executed from $8kHz$ to $12kHz$. A driving voltage of $1.5V$ was applied in the injected sine wave signal. The test actuation scheme was the same as in Section 5.1.2.

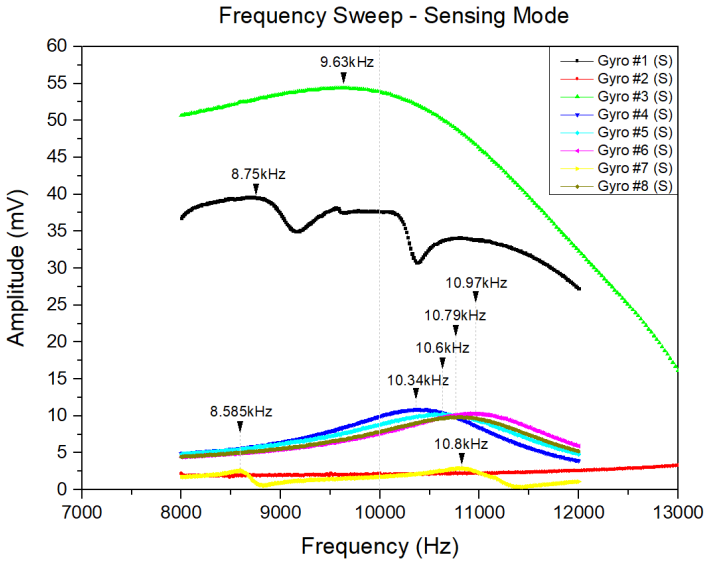

Figure 5.8: Plot of the frequency sweep - sense mode response.

It is worth nothing that since some gyroscopes present multiple peaks, in Table 5.5 only the peaks with the highest amplitude were considered.

Firstly gyroscope #1 presents 3 oscillation modes in this range - the highest amplitude peak is located at $8.75kHz$, the second one at $9.568kHz$, and lastly another at $10.839kHz$. The presence of multiple peaks in this range hints at a faulty fabrication process or defects introduced during the packaging and bonding process. Comparing the frequency sweep to the other $40\mu m$ device (gyroscope #3) which presents a single amplitude peak

Table 5.5: Frequency response of the sensing mode.

Device	Expected Peak (Hz)	Real Peak (Hz)	Δ Frequency (Hz)
Gyro #1 (40μm)	10134	8749 / 9568	1385 / 566
Gyro #2 (100μm)	10027	No peak	NaN
Gyro #3 (40μm)	10106	9625	481
Gyro #4 (100μm)	10032	10349	317
Gyro #5 (100μm)	10032	10621	589
Gyro #6 (100μm)	10027	10978	951
Gyro #7 (100μm)	10019	10839	820
Gyro #8 (100μm)	10019	10796	777

at 9.63kHz, corroborates this hypothesis.

While gyroscope #2 presents no detectable peak, all the other 100μm devices present a clear wide peak after the 10kHz mark. Moreover, gyroscope #7 presents an additional vibration mode at 8.585kHz. Another important remark is that, even though the peaks are well defined, their amplitude is lower than the 40μm counterparts. This performance gap may translate into a non-readable signal due to multiple reasons:

1. The resonant peak of the sensing mode is too distant from the resonant peak of the driving mode, resulting in a bad transfer rate between the modes.

2. The circuit noise could be above the threshold where it is possible to observe a response. The Coriolis Effect might not be able to excite the secondary mode of oscillation to the point where it produces a readable measurement.

The phase behaviour of the oscillators can be checked in Appendix C. The gyroscopes which presented a faulty fabrication, also show irregular phase performance.

5.3 Noise measurements

Sensors never produce an electric response that perfectly reflects the input stimulus's ideal representation. These deviations or unwanted excitations that translate into errors in the output signal are considered noise [44].

These distortions can either be systematic or stochastic. In the first case, these errors are related to the sensor's quality, design, transfer function, dynamic characteristics, and calibration - during short periods, they are predictable and consistent. Therefore they can be characterized and be subtracted from the output response through various methods. On the other hand, stochastic disturbances are unpredictable, don't converge, and are inherently irregular [1].

It is important therefore to determine the noise characteristics of the used circuits, to determine if the output signal is obfuscated by these unwanted interference's.

5.3.1 Circuit Noise and Quadrature Error Influence

The noise measurements were made with the MNS Gyro Evaluation Board, using the UHFLI 600 MHz Lock-in Amplifier from Zurich Instruments, by applying the Sweeper Mode with a Noise Amplitude Sweep function. The injected driving signal was a sine wave with a 1.5V amplitude to the drive mode's actuation comb fingers. The output response was taken from the sensing comb fingers of the sense mode.

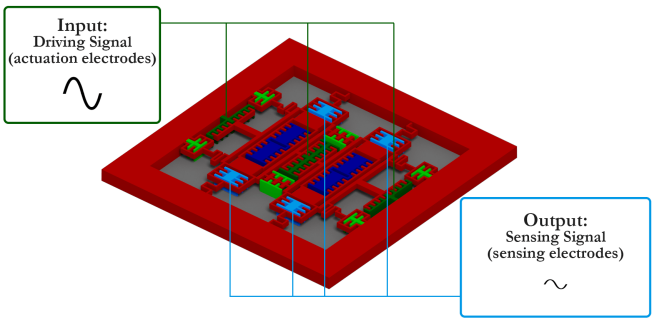

Figure 5.9: Illustration of the test actuation scheme for the noise measurements.

A preliminary noise test was realized. A MEMS Gyroscope operation always involves a power supply, an injected carrier wave, and a driving signal. Therefore, seeing the cumulative effect of each on the output spectrum response allows to assess each noise source's impact.

Table 5.6: Preliminary noise sources test values for the MNS Gyro Evaluation Board.

Power Supply	Carrier Wave	Driving Signal	Zero Rate Offset
+12V / -12V	None	None	$49\mu V$
+12V / -12V	5V sin($2MHz$)	None	$225\mu V$
+12V / -12V	5V sin($2MHz$)	1.5V sin($10kHz$)	$4.08mV$

In figures 5.10 and 5.11 the noise floor of the circuit is considered without the driving signal actuation. The noise floor of this circuit is therefore in the order of single digit μV, which means that the signal would not be clouded in the intrinsic noise of the circuit itself. The $4.08mV$ Zero Rate Offset (ZRO) value is the response of the sensor when no input is applied - it is denominated by Bias, following the IEEE Standards [40].

As it is possible to see in Table 5.6, the major contributing factor to the rise of the output noise is the driving signal injection. As discussed in Section 2.2.2, this may be due to the presence of the quadrature error and the spillover of the drive dynamics into the sensing mode [45].

To confirm that hypothesis, an output response was extracted from the circuit while the driving mode signal was increased. Since the UHFLI 600 MHz Lock-in Amplifier can't output more than 1.5V, an Agilent 33250A signal generator was used. Therefore,

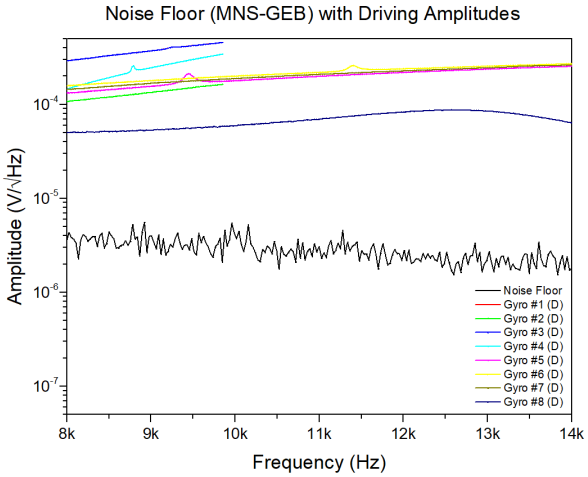

Figure 5.10: Illustration of the noise floor compared with the driving amplitude responses.

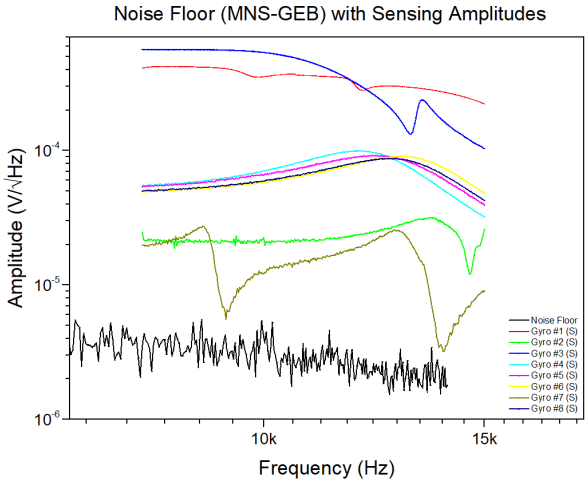

Figure 5.11: Illustration of the noise floor compared with the sensing amplitude responses.

the testing conditions were different compared to the ones used to the results achieved in Table 5.6.

First no driving signal was applied to get a baseline for the measurement. Then, the amplitude voltage was incremented to prove the connection between the quadrature error on the output signal and the driving signal. To realize this measurement, gyroscope #3 was used due to having the best driving amplitude. The values are listed in Table 5.7.

It is possible to conclude that the driving signal has a proportional relationship with the quadrature error. For an amplitude of $5V$, a total of $11mV$ of output can be introduced by the spillover. This highlights the need for a mechanism of cancellation of the quadrature error in order to achieve a better signal output.

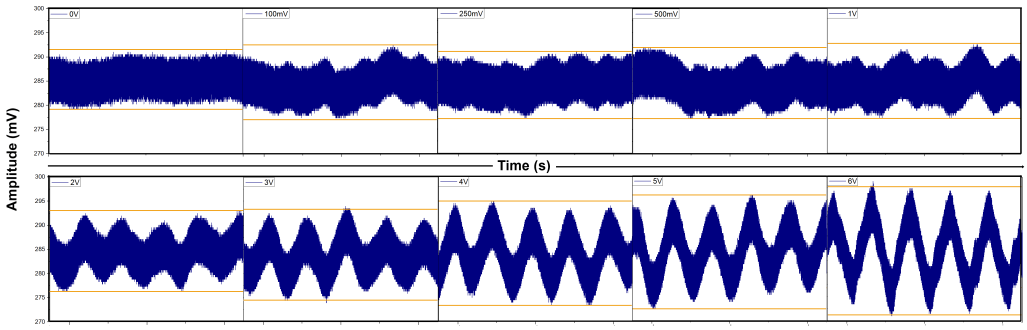

Figure 5.12: Illustration of the effect of the driving mode on the sensing output response due to the quadrature error.

Table 5.7: Sense Output increase due to Driving Voltage.

D-Signal Voltage	Min-Voltage (mV)	Max-Voltage (mV)	Amplitude (mV)
$0V$	278	290	12
$0.1V$	277	291	14
$0.25V$	277	290	13
$0.5V$	277	291	14
$1V$	277	291	14
$2V$	276	292	16
$3V$	273	293	20
$4V$	273	294	21
$5V$	272	295	23
$6V$	270	298	28

5.3.2 Allan Variance

The Allan Variance (AV) method is a time-domain analysis method developed to characterize high precision oscillators and clocks [46]. Since a MEMS Gyroscope is an inertial precision device that functions as a resonator, the AV method is an IEEE approved standard analysis method for characterizing these devices [47]. More specifically the Overlapping Allan Variance algorithm was utilized due to having the best performance / computation time relationship [48].

In short, the AV method is applied to a sequence of data points, and it has the following approach:

1. The time-domain data is divided into clusters of data, their standard deviation is operated upon an algorithm, and the Allan Variance is acquired;

2. The Allan Variance is taken from the previous data, and both axes are plotted in a Log-Log graph;

3. Based on the plot, three noise performance characteristics can be identified - the Angle Random Walk (ARW), the Rate Random Walk (RRW), and the Bias Stability.

To get the data an UHFLI 600 MHz Lock-in Amplifier was utilized. A Python script was developed to treat the data and to calculate the Allan Variance. The code can be retrieved in Appendix II. The in-depth explanation of this method can be read in Annex I.

Since the Allan Variance data gathering is a very time consuming process, only Gyroscope #1 and #3 were characterized. The MEMS devices were sampled at 800Hz (800 samples per second) during approximately 48 hours.

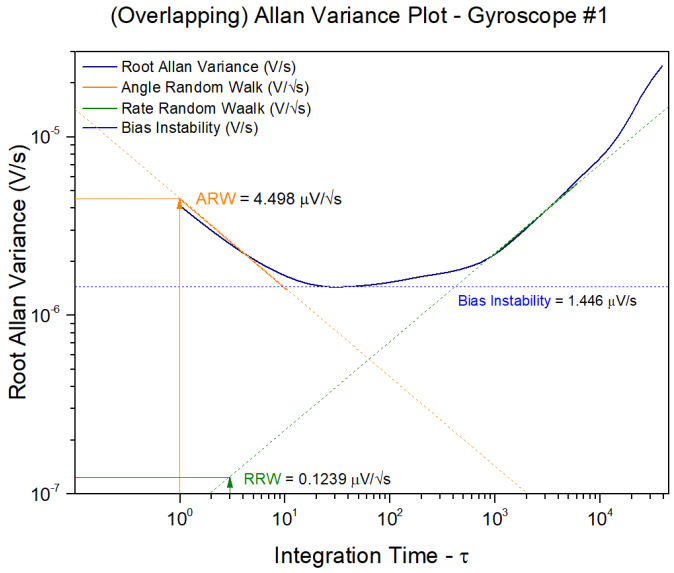

Figure 5.13: Log-Log Plot of the Root Allan Variance for Gyroscope #1 with noise performance metrics.

Table 5.8: Noise performance metrics of gyroscope #1 taken with the Allan Variance analysis.

ARW $(V/\sqrt{s})$	**Bias Stability** (V/s)	**RRW** $(V/\sqrt{s})$
$4.498\mu V/\sqrt{s}$	$1.446\mu V/s$	$0.1239\mu V/\sqrt{s}$

In order to analyze this graphic, some considerations have to be made:

The ARW is taken by the value at $\tau = 0$ with slope $-1/2$, therefore a linear fitting was made with the same fixed gradient to extract the exact data point.

The RRW is taken by the value at $\tau = 3$ in the slope $1/2$, therefore a linear fitting was made with a similar purpose explained above.

The Bias Stability value is the minimum y (Allan Deviation) value. It represents the convergence of the deviation to a stable value before the Rate Random Walk effects play into factor. It is the lowest possible deviation that the sensor can suffer [42].

The ARW is a measure of random white noise resulting from the output integration of the stationary gyroscope. The ideal value should be zero, which would mean that

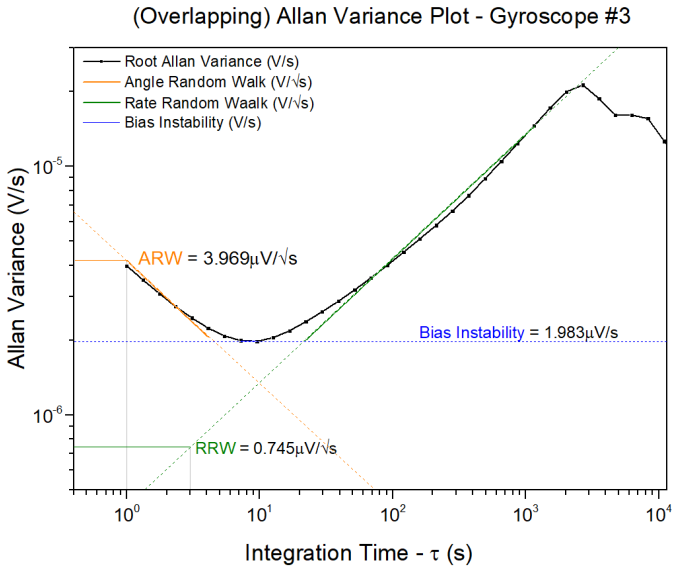

Figure 5.14: Log-Log Plot of the Allan Variance for Gyroscope #3 with noise performance metrics.

Table 5.9: Noise performance metrics of gyroscope #3 taken with the Allan Variance analysis.

ARW ($V/\sqrt{s}$)	**Bias Stability** (V/s)	**RRW** ($V/\sqrt{s}$)
$3.969\mu V/\sqrt{s}$	$1.983\mu V/s$	$0.745\mu V/\sqrt{s}$

the sensor would not output a different voltage over time for the same input rotation. Too much ARW reduces the measurement precision [49]. Its coefficient describes the average deviation that will occur due to this noise element. Since the value of gyroscope #1 ARW is $4.498\mu V/\sqrt{s}$ it means that while integrating the rotation of the gyroscope for ten seconds, the output deviates on average $0.223mV$. This value is taken from taking the squared ARW and multiplying it by the time frame of the measurement [50].

The RRW coefficient refers to the random walk noise component in the gyroscope rate output signal that is usually permanent in nature. It is caused by the accumulated errors in the mechanical dynamics of the MEMS, that will translate into a drift due to this process, in an average quantity equal to the $RRW\sqrt{\Delta t}$, where Δt is the time interval. This noise source is speculated to originate from the degradation of the MEMS, and materials contacting with the sensor and the circuit [51, 52].

The Bias Stability measures the output stability over a certain length of time, and is a fundamental performance metric of any MEMS inertial sensor. The value reflect the drift of the ZRO over time, which means that the output of the sensor would drift from Gyroscope #1 initial Bias randomly with a value of approximately $1.446\mu V/s$.

5.4 Phase Sensitive Demodulation

The Lock-In Amplifying method operates by multiplying an input signal with a parallel signal tuned to the frequency and phase of interest to demodulate. In a generalized form, an input signal consisting of a sinusoid with frequency w_{drive} is applied, while the lock-in amplifier is tuned to the same frequency. During the mixing process of the multiplier, an intermediate signal is generated [53]:

$$\begin{aligned} S_{intermediate} &= sin(w_{drive}t) \times sin(w_{drive}t) \\ &= \frac{A}{2} \times (cos(\Delta\phi) + cos(2w_{drive}t + \Delta\phi)) \end{aligned} \tag{5.2}$$

Since part of the mixing product is generated at twice the carrier frequency, by applying a low pass filter that same component can be rejected [54]. The output is a DC signal in the form of $\frac{A}{2} \times cos(\Delta\phi)$.

By applying this phase sensitive demodulation method to the Gyroscope output, theoretically the Quadrature Error could be rejected. A reminder that although the Quadrature Error and the Coriolis response occur at the same frequency but with a 90° phase shift (see Section 2.2.2), in the FFT reading they are superimposed, which adds difficulty in extracting a rotation response.

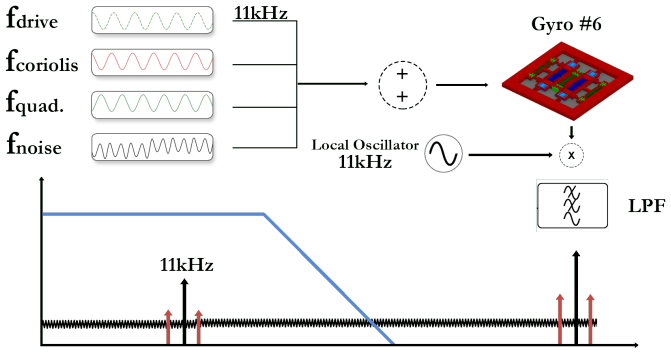

Figure 5.15: Illustration of the quadrature error frequency component being rejected.

Using as an example Gyroscope #6, which has its resonant peak of the sensing mode at $10.97kHz$, if a driving signal of 5V at $11kHz$ is applied to the driving mode, with a carrier wave signal of $2MHz$, then it would be possible to reject the quadrature signal.

To test this hypothesis, the MokuLab Lock In Amplifier was used to demodulate the quadrature signal. A sinusoidal wave of the same frequency as the output of the gyroscope was produced, with a 90° phase shift. It is possible to see in figure 5.16 that the amplitude of the sensor's output is $24.85mV$ before any demodulation occurs.

After the multiplication of both signals, a Low Pass Filter (LPF) with a stop frequency of 15kHz is applied. The signal doesn't suffer any other type of transformation.

As it is possible to understand through figure 5.17, by analyzing the signal at the output of the MokuLab (that is, the demodulated signal), it is possible to see that the

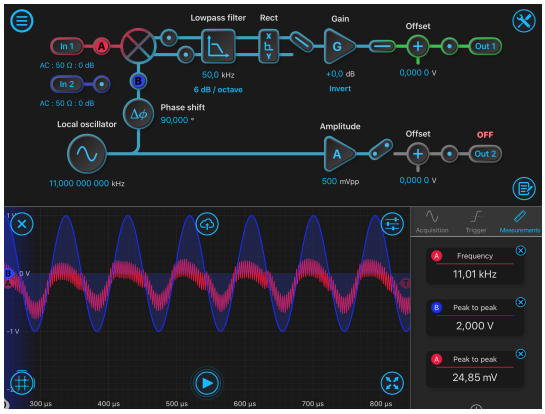

Figure 5.16: MokuLab Lock-In Amplifier - (A) Output Signal of the Gyroscope; (B) Local Oscillator at $11kHz$ overlying the quadrature signal.

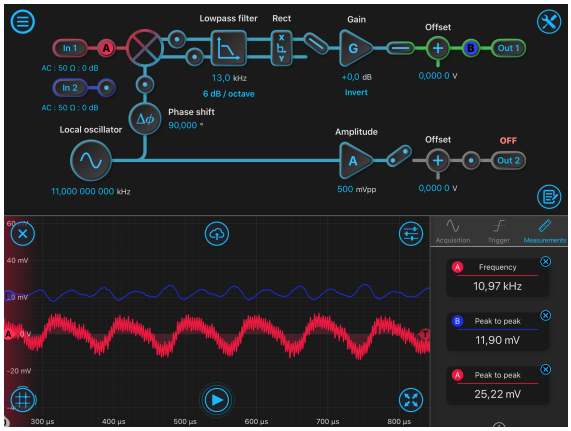

Figure 5.17: MokuLab Lock-In Amplifier - (A) Output Signal of the Gyroscope; (B) Output of the gyroscope after the demodulation of the signal.

amplitude of the output reduced in more than 50%, from $24.85mV$ to $11.90mV$. Still, the quadrature error partly persists. Typically, the phase demodulation occurs before the signal is processed by the circuit and the reference oscillator used to demodulate is the driving signal itself [23, 55]. Furthermore, the quadrature error is not mechanically cancelled. Therefore, the solution presented, while diminishing the noise of the unwanted excitation, is non-ideal.

5.5 Sensitivity

For sensitivity characterization of CVG devices to angular rate input, the gyroscopes are usually mounted on a rotation rate table.

The actuation scheme is the same as the one used for the Noise Measurements in Section 5.3.

The following test set up was utilized: A Thor Labs Rotation Stage with Stepper Motor, two Agilent E3610A DC Power Supply to feed the circuit, two Agilent 33250A Arbitraty Waveform Generators for drive and carrier wave signals, an oscilloscope to read

the output response, and the MNS Gyro Evaluation Board.

There are two forms to verify if the amplitude of signal is being modulated by the Coriolis force - using the time domain response or the frequency domain response. In figure 5.18 it is possible to see what is the desired response upon a rotation on both domains. In spite of the result demonstrated, other types of vibration (hitting the table, physical touches on the PCB board) also produce a similar response, making it hard to validate if the amplitude modulation is being caused by the Coriolis effect.

By using the Fast Fourier Transform (FFT) option on the oscilloscope, it is possible to see the frequency response of the device. Since the sensing mode frequency is known, it is possible to determine if the Coriolis effect is causing the modulation by exciting the expected vibratory mode.

Figure 5.18: Illustration of Amplitude Modulation using the FFT mode on the oscilloscope.

Even though some modulation was able to be seen, its increase isn't drastic enough even after a phase sensitive demodulation of the quadrature signal (see Section 5.4). Furthermore, this result required aggressive rotation rates. Figure 5.18 was obtained using the Gyroscope #3, which has the best dynamic performance. The used driving signal was a $5V$ sine wave at $9.6kHz$ in order to take advantage of the resonant peak of Gyroscope #3 sensing mode (see Table 5.5).

For small rotation rates, no response was obtained. This indicates that the tested devices may not have the performance characteristics that allow for the easy extraction of the rotation signal. Since the sensor was tested in open air, and it is not hermetically packaged, it could also mean that the damping critically inhibits the sensing mode oscillation. The device wasn't tested in vacuum due to the impossibility of rotating it under low pressure conditions given the lack of a proper equipment setup.

Since the results obtained were hardly reproducible, and coherent, they were not added to this section.

Chapter

6 Conclusions and Future Perspectives

MEMS Capacitive Vibratory Gyroscopes are inertial sensors that require extensive characterization in order to evaluate their performance. Due to their complexity, several factors may influence its functioning: from design choices, fabrication imperfections, packaging, supporting circuits, to environmental factors. This study identified some of the critical parameters of eight dual-mass MEMS CVG.

By realizing rate transfer tests, an understanding of each resonant mode of the gyroscopes' behaviour was gathered. These transfer tests are the baseline of the characterization process, not only to see the dynamic amplitude of the resonating devices but also to validate their fabrication. An oscillation mode that cannot be actuated and measured translates to a non-functioning gyroscope.

Under the same testing conditions, the $40\mu m$ devices had greater driving and sensing amplitudes due to the decreased thickness of their suspended parts. Even though a bigger proof mass is preferred to increase sensitivity, the performance of the $100\mu m$ devices presented at least a 590% sense-mode transfer rate performance gap to the Gyroscope #3.

The frequency and phase sweeping tests followed in order to further substantiate the fabrication procedure. Since the tested devices were modelled to have specific resonant frequencies, the mismatch between the predicted and real values was analyzed. Although the disparity never exceeded 11%, there is room for improvement with better fabrication procedures. In order to achieve better performance from frequency-mismatched gyroscopes, w_x and w_y need to be as close as possible to the expected values [56]. The phase behaviour of the gyroscopes proved to be expected for each resonator.

Afterwards, the noise performance characteristics of the system were acquired. A baseline measure of the circuit noise was extracted, revealing that the electronics' noise floor was not restricting the Coriolis response withdrawal. Furthermore, the spillover effect of the quadrature error from the drive mode dynamics (from 0 to 5V) was tested for gyroscope #3, resulting in a 91.7% increase of the ZRO / Bias. Three major noise performance characteristics were retrieved using the Allan Variance method. Python was utilized to treat and analyze the data.

On the other hand, the sensitivity test was unsuccessful, meaning that no consistent Coriolis response was extracted. This may be due to the sensors' inadequate packaging,

which exhibits similar performance to gyroscopes that weren't hermetically encapsulated. This reduction of the Q factor due to the oscillatory mode's critical damping, plus the non-cancelled quadrature error, contributes to a severely deteriorated sense-mode performance. The lack of a sensitivity measure does not allow the translation of units from V to degrees per time unit, which is the standard.

To conclude the sensor testing, a phase-sensitive demodulation of the quadrature error was tried. The quadrature response of the signal was reduced. The usage of a local oscillator to demodulate the signal is still an inferior solution compared to the methodology presented in the literature, based on the usage of the driving signal itself, with a phase shift of 90° to cancel this unwanted component.

With an appropriate testing setup, it would be possible to measure behaviour under different temperatures to assess the thermal linearity of the sensor. MEMS Gyroscopes are prone to performance fluctuations under different ambient conditions, usually requiring additional control electronics for compensation [57].

Moreover, a prototype circuit that is planned to operate in a closed-loop using an ASIC was fabricated. Even though the circuit itself was not validated in this work, the PCB Layout methodology presented is transferable to every circuit related to sensing applications; therefore it was included.

To be more successful in future testing projects, a rotating table capable of being operated in both directions and fitted in the vacuum chamber is of the utmost importance. The miniaturization of the MNS Gyro Evaluation Board is also critical for testing under lower-pressure conditions, since the current dimensions do not allow such characterization. The proposed prototype board has a third of the used board size and is prepared to be integrated with the existing vacuum chamber setup through a D-SUB connection. The characterization of the conventional MEMS gyroscope for comparison was not possible during this project due to the lack of more LCC in which to integrate it - highlighting the need for alternative circuits which accommodate multiple bonding options. For that reason, two versions of the prototyped board were developed.

In conclusion, the developed work lays the foundations for testing future devices that will return better, faster and more accurate performance metrics. Efforts to automate the extraction and analysis of more characterization measurements should be employed in the future. After improving the aforementioned, opportunities to break state of the art present themselves:

- By exploring alternative and more complex electronic control and signal processing circuits;
- By investigating new design options for gyroscopes which take advantage of novel or improved sensing mechanisms;
- By employing optimization algorithms in the design process of the sensors to obtain the devices' peak performance parameters.

Bibliography

[1] S. Beeby et al. *MEMS Mechanical Sensors*. Artech House, 2004 (cit. on pp. 1, 3, 24).

[2] A. A. Trusov. "Overview of MEMS gyroscopes: history, principles of operations, types of measurements". In: *University of California, Irvine, USA* (2011) (cit. on pp. 1, 5, 6, 9).

[3] C. Acar and A. Shkel. *MEMS vibratory gyroscopes: structural approaches to improve robustness*. Springer Science & Business Media, 2008 (cit. on pp. 1, 3, 5, 8–10, 22).

[4] H. Xie and G. K. Fedder. "Integrated microelectromechanical gyroscopes". In: *Journal of aerospace engineering* 16.2 (2003), pp. 65–75 (cit. on p. 1).

[5] *IEEE Standard for Inertial Sensor Terminology*. DOI: 10.1109/ieeestd.2001.93360. URL: https://doi.org/10.1109/ieeestd.2001.93360 (cit. on p. 3).

[6] V. M. N. Passaro et al. "Gyroscope Technology and Applications: A Review in the Industrial Perspective". In: *Sensors* 17.10 (Oct. 2017), p. 2284. DOI: 10.3390/s17102284. URL: https://doi.org/10.3390/s17102284 (cit. on pp. 3, 9).

[7] D. Liu et al. "Research on temperature dependent characteristics and compensation methods for digital gyroscope". In: *2008 3rd International Conference on Sensing Technology*. IEEE, Nov. 2008. DOI: 10.1109/icsenst.2008.4757112. URL: https://doi.org/10.1109/icsenst.2008.4757112 (cit. on p. 3).

[8] Y. Ni, H. Li, and L. Huang. "Design and Application of Quadrature Compensation Patterns in Bulk Silicon Micro-Gyroscopes". In: *Sensors* 14.11 (Oct. 2014), pp. 20419–20438. DOI: 10.3390/s141120419. URL: https://doi.org/10.3390/s141120419 (cit. on p. 3).

[9] Q. Shi et al. "Design Principle of Suspension of MEMS Gyroscope". In: *2006 1st IEEE International Conference on Nano/Micro Engineered and Molecular Systems*. IEEE, Jan. 2006. DOI: 10.1109/nems.2006.334695. URL: https://doi.org/10.1109/nems.2006.334695 (cit. on p. 3).

[10] A. A. Trusov, A. R. Schofield, and A. M. Shkel. "Performance characterization of a new temperature-robust gain-bandwidth improved MEMS gyroscope operated in air". In: *Sensors and Actuators A: Physical* 155.1 (Oct. 2009), pp. 16–22. DOI: 10.1016/j.sna.2008.11.003. URL: https://doi.org/10.1016/j.sna.2008.11.003 (cit. on p. 3).

[11] Y. Su et al. "The Characteristics and Locking Process of Nonlinear MEMS Gyroscopes". In: *Micromachines* 11.2 (Feb. 2020), p. 233. DOI: 10.3390/mi11020233. URL: https://doi.org/10.3390/mi11020233 (cit. on p. 3).

[12] X. Liu, D. Chen, and K. Song. "A low-noise readout interface for silicon MEMS vibratory gyroscope". In: *Modern Physics Letters B* 35.03 (Oct. 2020), p. 2150069. DOI: 10.1142/s021798492150069x. URL: https://doi.org/10.1142/s021798492150069x (cit. on p. 4).

[13] A. Norouzpour-Shirazi, M. F. Zaman, and F. Ayazi. "A Digital Phase Demodulation Technique for Resonant MEMS Gyroscopes". In: *IEEE Sensors Journal* 14.9 (Sept. 2014), pp. 3260–3266. DOI: 10.1109/jsen.2014.2326974. URL: https://doi.org/10.1109/jsen.2014.2326974 (cit. on p. 4).

[14] G. Zhanshe et al. "Research development of silicon MEMS gyroscopes: a review". In: *Microsystem Technologies* 21.10 (Aug. 2015), pp. 2053–2066. DOI: 10.1007/s00542-015-2645-x. URL: https://doi.org/10.1007/s00542-015-2645-x (cit. on p. 4).

[15] J. Oprea. "Geometry and the Foucault Pendulum". In: *The American Mathematical Monthly* 102.6 (June 1995), pp. 515–522. DOI: 10.1080/00029890.1995.12004611. URL: https://doi.org/10.1080/00029890.1995.12004611 (cit. on p. 4).

[16] A. D. Aczel and R. H. Romer. "PENDULUM-Léon Foucault and the Triumph of Science". In: *American Journal of Physics* 72.2 (Feb. 2004), pp. 286–287. DOI: 10.1119/1.1637901. URL: https://doi.org/10.1119/1.1637901 (cit. on p. 4).

[17] R. Haberfellner et al. *Systems Engineering*. Springer International Publishing, 2019. DOI: 10.1007/978-3-030-13431-0. URL: https://doi.org/10.1007/978-3-030-13431-0 (cit. on p. 5).

[18] C. Patel and P. McCluskey. "Modeling and simulation of the MEMS vibratory gyroscope". In: *13th InterSociety Conference on Thermal and Thermomechanical Phenomena in Electronic Systems*. IEEE, May 2012. DOI: 10.1109/itherm.2012.6231524. URL: https://doi.org/10.1109/itherm.2012.6231524 (cit. on p. 5).

[19] S. Park and R. Horowitz. "Adaptive control for the conventional mode of operation of mems gyroscopes". In: *Journal of Microelectromechanical Systems* 12.1 (Feb. 2003), pp. 101–108. DOI: 10.1109/jmems.2002.807468. URL: https://doi.org/10.1109/jmems.2002.807468 (cit. on p. 6).

[20] Z. Instruments. *Control of MEMS Coriolis Vibratory Gyroscopes*. 2015. URL: https://www.zhinst.com/sites/default/files/zi_appnote_mems_gyroscope.pdf (cit. on pp. 7, 8).

[21] F. Chen et al. "Design and Implementation of an Optimized Double Closed-Loop Control System for MEMS Vibratory Gyroscope". In: *IEEE Sensors Journal* 14.1 (Jan. 2014), pp. 184–196. DOI: 10.1109/jsen.2013.2271586 (cit. on p. 7).

[22] V. Apostolyuk. *Coriolis Vibratory Gyroscopes*. Springer International Publishing, 2016. DOI: 10.1007/978-3-319-22198-4. URL: https://doi.org/10.1007/978-3-319-22198-4 (cit. on p. 7).

[23] E. Tatar, S. E. Alper, and T. Akin. "Quadrature-Error Compensation and Corresponding Effects on the Performance of Fully Decoupled MEMS Gyroscopes". In: *Journal of Microelectromechanical Systems* 21.3 (June 2012), pp. 656–667. DOI: 10.1109/jmems.2012.2189356. URL: https://doi.org/10.1109/jmems.2012.2189356 (cit. on pp. 7, 8, 31).

[24] J. Geen et al. "Single-chip surface micromachined integrated gyroscope with 50°/h Allan deviation". In: *IEEE Journal of Solid-State Circuits* 37.12 (Dec. 2002), pp. 1860–1866. DOI: 10.1109/jssc.2002.804345. URL: https://doi.org/10.1109/jssc.2002.804345 (cit. on p. 8).

[25] A. Sharma et al. "A 0.1degree$\sqrt{Hz}$ bias drift electronically matched tuning fork microgyroscope". In: *2008 IEEE 21st International Conference on Micro Electro Mechanical Systems*. IEEE, Jan. 2008. DOI: 10.1109/memsys.2008.4443579. URL: https://doi.org/10.1109/memsys.2008.4443579 (cit. on p. 8).

[26] J. Raman et al. "A Closed-Loop Digitally Controlled MEMS Gyroscope With Unconstrained Sigma-Delta Force-Feedback". In: *IEEE Sensors Journal* 9.3 (Mar. 2009), pp. 297–305. DOI: 10.1109/jsen.2008.2012237. URL: https://doi.org/10.1109/jsen.2008.2012237 (cit. on p. 8).

[40] *IEEE Standard Specification Format Guide and Test Procedure for Coriolis Vibratory Gyros*. DOI: 10.1109/ieeestd.2004.95744. URL: https://doi.org/10.1109/ieeestd.2004.95744 (cit. on pp. 9, 17, 25, 56).

[27] J. Geen. "Progress in integrated gyroscopes". In: *IEEE Aerospace and Electronic Systems Magazine* 19.11 (Nov. 2004), pp. 12–17. DOI: 10.1109/maes.2004.1365660. URL: https://doi.org/10.1109/maes.2004.1365660 (cit. on p. 10).

[28] R. Neul et al. "Micromachined Angular Rate Sensors for Automotive Applications". In: *IEEE Sensors Journal* 7.2 (Feb. 2007), pp. 302–309. DOI: 10.1109/jsen.2006.888610. URL: https://doi.org/10.1109/jsen.2006.888610 (cit. on p. 10).

[29] T. E. Oliphant. "Python for scientific computing". In: *Computing in Science & Engineering* 9.3 (2007), pp. 10–20 (cit. on p. 12).

[30] *Pandas Python Library - a fast, powerful, flexible and easy to use open source data analysis and manipulation tool*. Accessed: 2020-02-22. URL: https://pandas.pydata.org/ (cit. on p. 12).

[31] *NumPy - an open source project aiming to enable numerical computing with Python*. Accessed: 2020-02-22. URL: https://numpy.org/ (cit. on p. 12).

[32] *AllanTools - Python Library for Allan deviation and related time/frequency statistics*. Accessed: 2020-02-13. URL: https://pypi.org/project/AllanTools/ (cit. on p. 12).

[33] B. J. Hosticka. "Analog circuits for sensors". In: *ESSCIRC 2007 - 33rd European Solid-State Circuits Conference*. IEEE, Sept. 2007. DOI: 10.1109/esscirc.2007.4430255. URL: https://doi.org/10.1109/esscirc.2007.4430255 (cit. on p. 13).

[34] R. Saleh et al. "System-on-Chip: Reuse and Integration". In: *Proceedings of the IEEE* 94.6 (June 2006), pp. 1050–1069. DOI: 10.1109/jproc.2006.873611. URL: https://doi.org/10.1109/jproc.2006.873611 (cit. on p. 13).

[35] A. D. Marcellis and G. Ferri. *Analog Circuits and Systems for Voltage-Mode and Current-Mode Sensor Interfacing Applications*. Springer Netherlands, 2011. DOI: 10.1007/978-90-481-9828-3. URL: https://doi.org/10.1007/978-90-481-9828-3 (cit. on pp. 13, 16).

[36] B. Almutairi. "Multi Stage Noise Shaping (MASH) Sigma Delta Modulator for Capacitive MEMS Inertial Sensors". PhD thesis. Faculty of Physical Science and Engineering: University of Southampton, Feb. 2015 (cit. on p. 14).

[37] J. Fraden. *Handbook of Modern Sensors*. Springer New York, 2010. DOI: 10.1007/978-1-4419-6466-3. URL: https://doi.org/10.1007/978-1-4419-6466-3 (cit. on pp. 14, 53, 54).

[38] G. Harman. *Wire bonding in microelectronics*. McGraw-Hill Education, 2010 (cit. on p. 15).

[39] A. Weiler and A. Pakosta. "High-speed layout guidelines". In: *Texas Instrumensts, Tech. Rep.* (2006) (cit. on p. 16).

[41] W. Li et al. "Enhanced temperature stability of sensitivity for MEMS gyroscope based on frequency mismatch control". In: *Microsystem Technologies* 23.8 (2017), pp. 3311–3317 (cit. on p. 17).

[42] G. A. Aydemir and A. Saranlı. "Characterization and calibration of MEMS inertial sensors for state and parameter estimation applications". In: *Measurement* 45.5 (June 2012), pp. 1210–1225. DOI: 10.1016/j.measurement.2012.01.015. URL: https://doi.org/10.1016/j.measurement.2012.01.015 (cit. on pp. 17, 28).

[43] S. Schmid, L. G. Villanueva, and M. L. Roukes. *Fundamentals of Nanomechanical Resonators*. Springer International Publishing, 2016. DOI: 10.1007/978-3-319-28691-4. URL: https://doi.org/10.1007/978-3-319-28691-4 (cit. on pp. 21, 22).

[44] D. A. Bies, C. Hansen, and C. Howard. *Engineering noise control*. CRC press, 2017 (cit. on p. 24).

[45] W.-T. Sung et al. "Design and performance test of a MEMS vibratory gyroscope with a novel AGC force rebalance control". In: *Journal of Micromechanics and Microengineering* 17.10 (Aug. 2007), pp. 1939–1948. DOI: 10.1088/0960-1317/17/10/003. URL: https://doi.org/10.1088/0960-1317/17/10/003 (cit. on p. 25).

[46] D. W. Allan and J. A. Barnes. "A MODIFIED "ALLAN VARIANCE"WITH INCREASED OSCILLATOR CHARACTERIZATION ABILITY". In: (1981) (cit. on pp. 27, 55).

[47] R. K. Curey et al. "Proposed IEEE inertial systems terminology standard and other inertial sensor standards". In: *PLANS 2004. Position Location and Navigation Symposium (IEEE Cat. No. 04CH37556)*. IEEE. 2004, pp. 83–90 (cit. on p. 27).

[48] J. Li and J. Fang. "Not Fully Overlapping Allan Variance and Total Variance for Inertial Sensor Stochastic Error Analysis". In: *IEEE Transactions on Instrumentation and Measurement* 62.10 (Oct. 2013), pp. 2659–2672. DOI: 10.1109/tim.2013.2258769. URL: https://doi.org/10.1109/tim.2013.2258769 (cit. on p. 27).

[49] D. Yuan et al. "Statistical Modeling of Random Walk Errors for Triaxial Rate Gyros". In: *IEEE Transactions on Instrumentation and Measurement* 65.2 (Feb. 2016), pp. 286–296. DOI: 10.1109/tim.2015.2450358. URL: https://doi.org/10.1109/tim.2015.2450358 (cit. on p. 29).

[50] M. Vagner. *MEMS GYROSCOPE PERFORMANCE COMPARISON USING ALLAN VARIANCE METHOD*. 2012. URL: http://home.engineering.iastate.edu/~shermanp/AERE432/lectures/Rate\%20Gyros/14-xvagne04.pdf (cit. on p. 29).

[51] L. C. Ng and D. J. Pines. "Characterization of ring laser gyro performance using the Allan variance method". In: *Journal of Guidance, Control, and Dynamics* 20.1 (1997), pp. 211–214 (cit. on pp. 29, 57).

[52] Q. Lam et al. "Gyro modeling and estimation of its random noise sources". In: *AIAA Guidance, Navigation, and Control Conference and Exhibit*. 2003, p. 5562 (cit. on p. 29).

[53] W. Yang. "Teaching phase-sensitive demodulation for signal conditioning to undergraduate students". In: *American Journal of Physics* 78.9 (2010), pp. 909–915 (cit. on p. 30).

[54] D. Blair and P. Sydenham. "Phase sensitive detection as a means to recover signals buried in noise". In: *Journal of Physics E: Scientific Instruments* 8.8 (1975), p. 621 (cit. on p. 30).

[55] H. Cao et al. "Optimization and experimentation of dual-mass MEMS gyroscope quadrature error correction methods". In: *Sensors* 16.1 (2016), p. 71 (cit. on p. 31).

[56] E Tatar, T Mukherjee, and G. Fedder. "Nonlinearity tuning and its effects on the performance of a MEMS gyroscope". In: *2015 Transducers-2015 18th International Conference on Solid-State Sensors, Actuators and Microsystems (TRANSDUCERS)*. IEEE. 2015, pp. 1133–1136 (cit. on p. 33).

[57] F. Jiancheng and L. Jianli. "Integrated model and compensation of thermal errors of silicon microelectromechanical gyroscope". In: *IEEE Transactions on instrumentation and measurement* 58.9 (2009), pp. 2923–2930 (cit. on p. 34).

[58] J. W. David Halliday Robert Resnick. *Fundamentals of Physics Extended*. 10th Edition. Wiley, 2013. ISBN: 9781118230725 (cit. on p. 53).

[59] L.-C. T. Simon Konge Koldbæk. "Improving MEMS Gyroscope Performance using Homogeneous Sensor Fusion". MA thesis. Denmark: Aalborg Universitet, May 2011 (cit. on pp. 55–57).

Appendix

A Driving and Sensing Signal Measurements

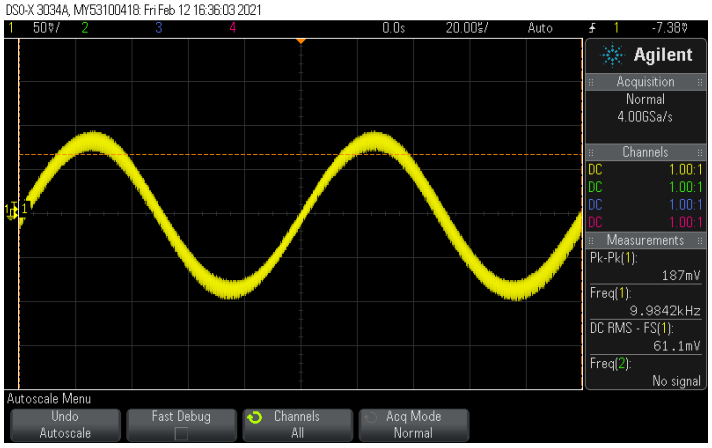

Figure A.1: Oscilloscope measurement of the drive amplitude - Gyroscope #1. Testing conditions: $A_{drive} = 5V$ / $f = 10kHz$

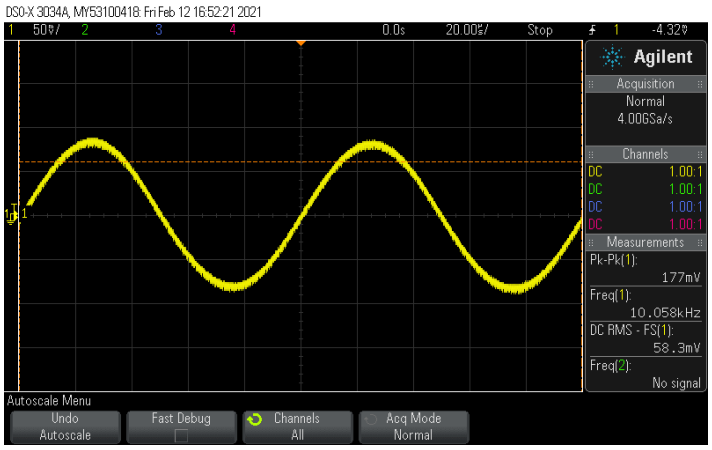

Figure A.2: Oscilloscope measurement of the drive amplitude - Gyroscope #2. Testing conditions: $A_{drive} = 5V$ / $f = 10kHz$

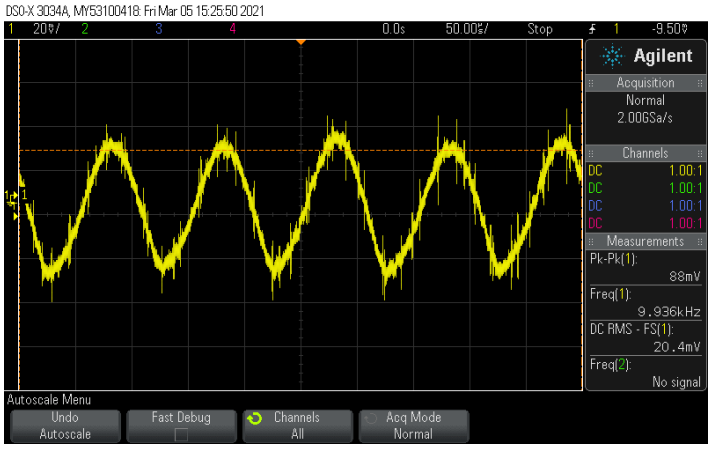

Figure A.3: Oscilloscope measurement of the drive amplitude - Gyroscope #3. Testing conditions: $A_{drive} = 5V$ / $f = 10kHz$

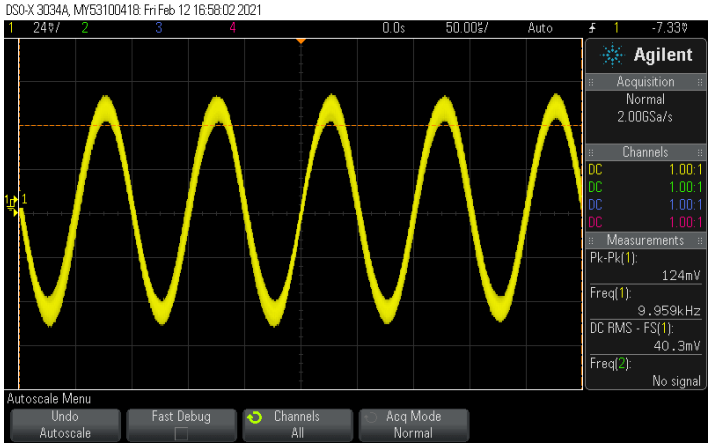

Figure A.4: Oscilloscope measurement of the drive amplitude - Gyroscope #4. Testing conditions: $A_{drive} = 5V$ / $f = 10kHz$

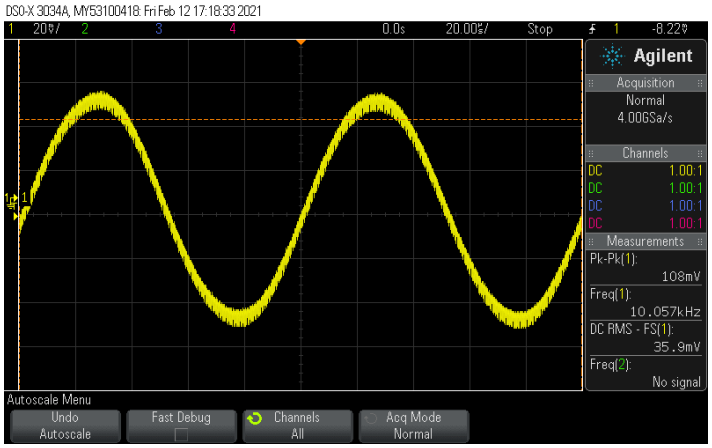

Figure A.5: Oscilloscope measurement of the drive amplitude - Gyroscope #5. Testing conditions: $A_{drive} = 5V$ / $f = 10kHz$

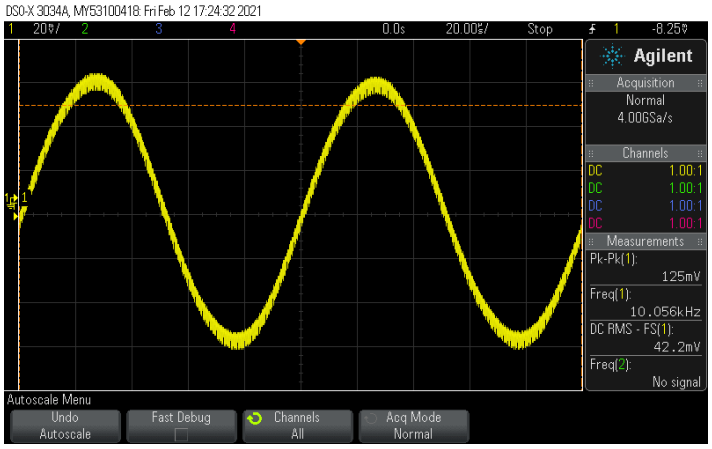

Figure A.6: Oscilloscope measurement of the drive amplitude - Gyroscope #6. Testing conditions: $A_{drive} = 5V$ / $f = 10kHz$

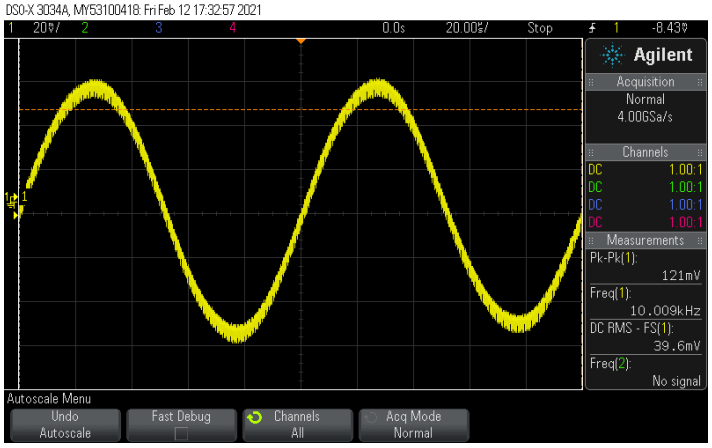

Figure A.7: Oscilloscope measurement of the drive amplitude - Gyroscope #7. Testing conditions: $A_{drive} = 5V$ / $f = 10kHz$

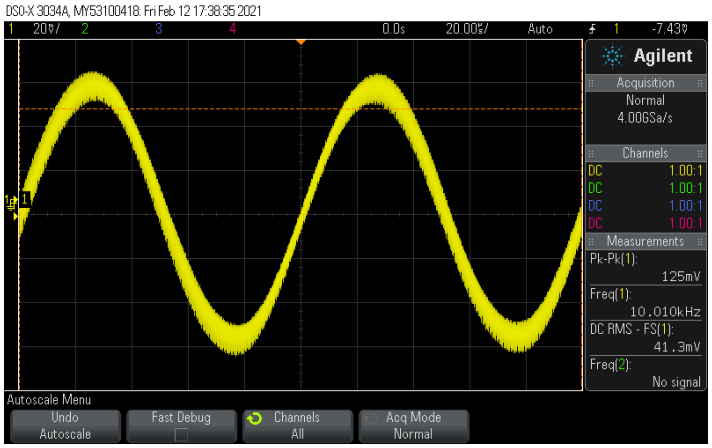

Figure A.8: Oscilloscope measurement of the drive amplitude - Gyroscope #8. Testing conditions: $A_{drive} = 5V$ / $f = 10kHz$

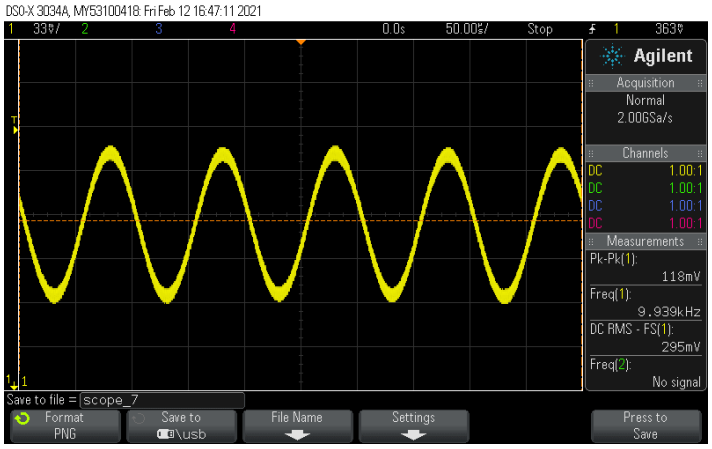

Figure A.9: Oscilloscope measurement of the sense amplitude - Gyroscope #1. Testing conditions: $A_{sense} = 5V$ / $f = 10kHz$

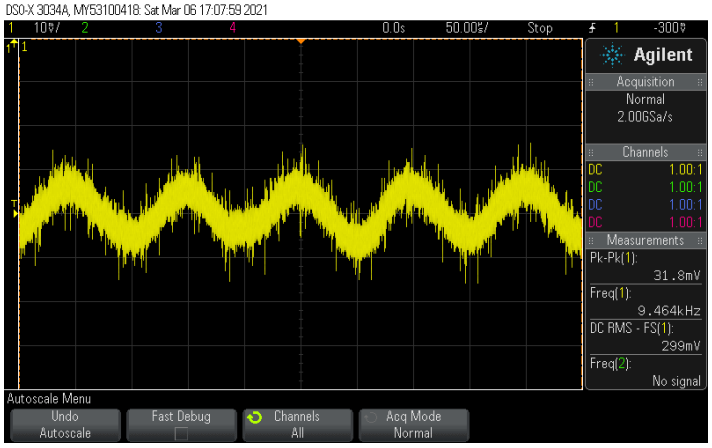

Figure A.10: Oscilloscope measurement of the sense amplitude - Gyroscope #2. Testing conditions: $A_{sense} = 5V$ / $f = 10kHz$

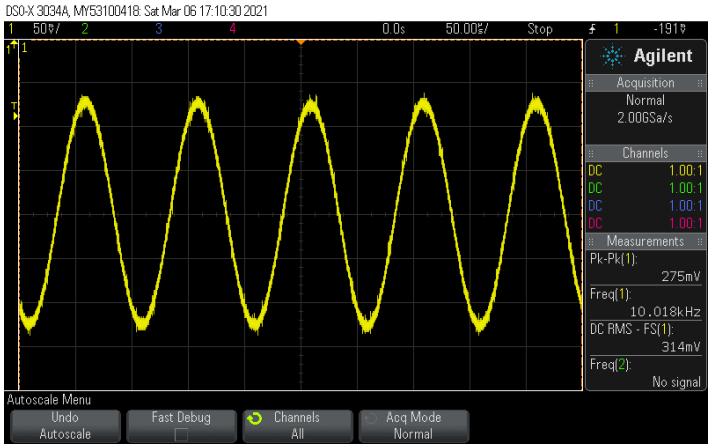

Figure A.11: Oscilloscope measurement of the sense amplitude - Gyroscope #3. Testing conditions: $A_{sense} = 5V$ / $f = 10kHz$

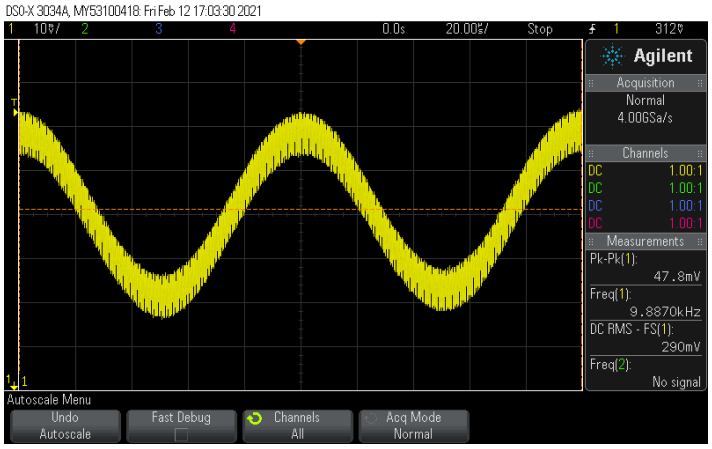

Figure A.12: Oscilloscope measurement of the sense amplitude - Gyroscope #4. Testing conditions: $A_{sense} = 5V$ / $f = 10kHz$

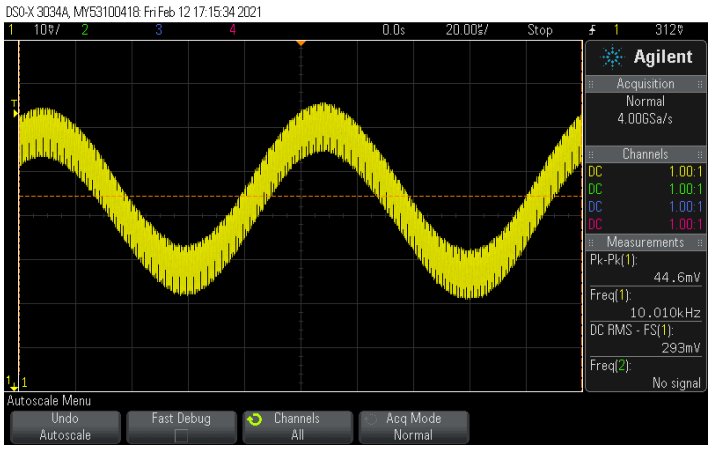

Figure A.13: Oscilloscope measurement of the sense amplitude - Gyroscope #5. Testing conditions: $A_{sense} = 5V$ / $f = 10kHz$

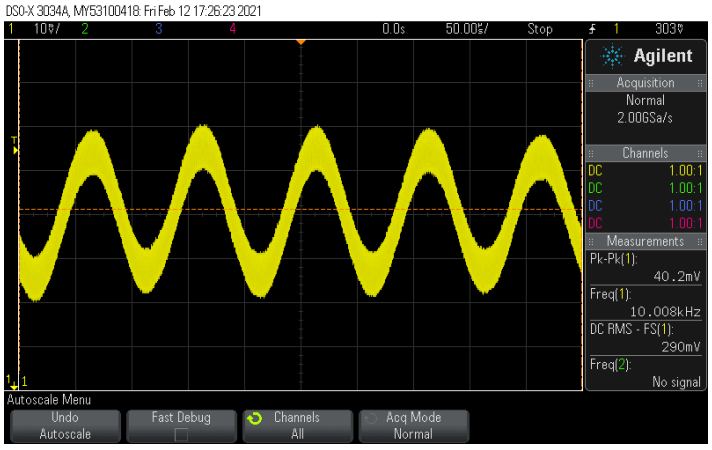

Figure A.14: Oscilloscope measurement of the sense amplitude - Gyroscope #6. Testing conditions: $A_{sense} = 5V$ / $f = 10kHz$

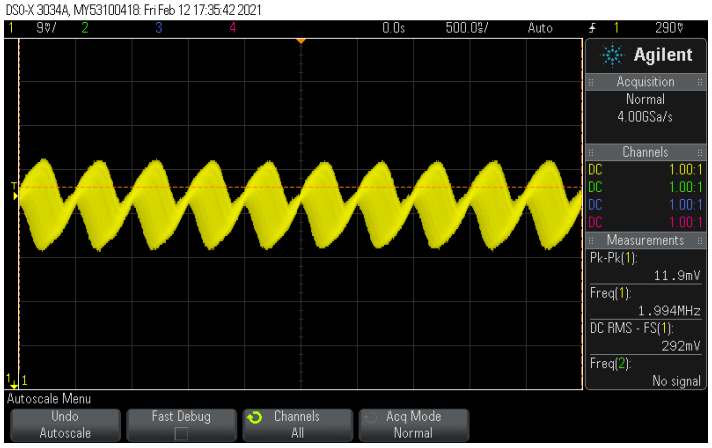

Figure A.15: Oscilloscope measurement of the sense amplitude - Gyroscope #7. Testing conditions: $A_{sense} = 5V$ / $f = 10kHz$

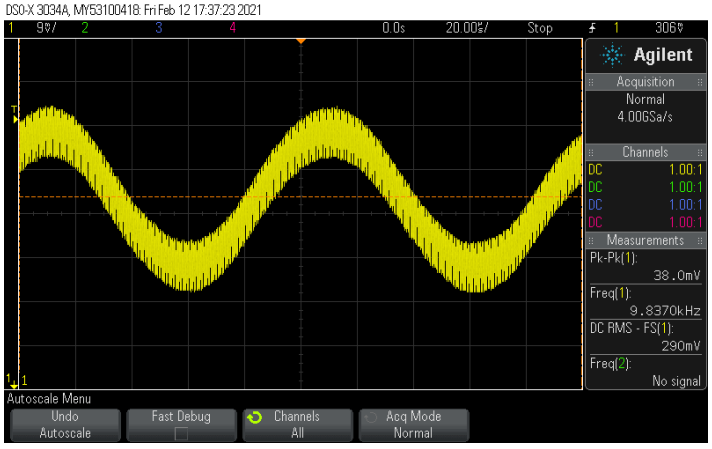

Figure A.16: Oscilloscope measurement of the sense amplitude - Gyroscope #8. Testing conditions: $A_{sense} = 5V$ / $f = 10kHz$

Appendix

B Noise Measurements

B.1 UHFLI Amplifier Noise Outputs

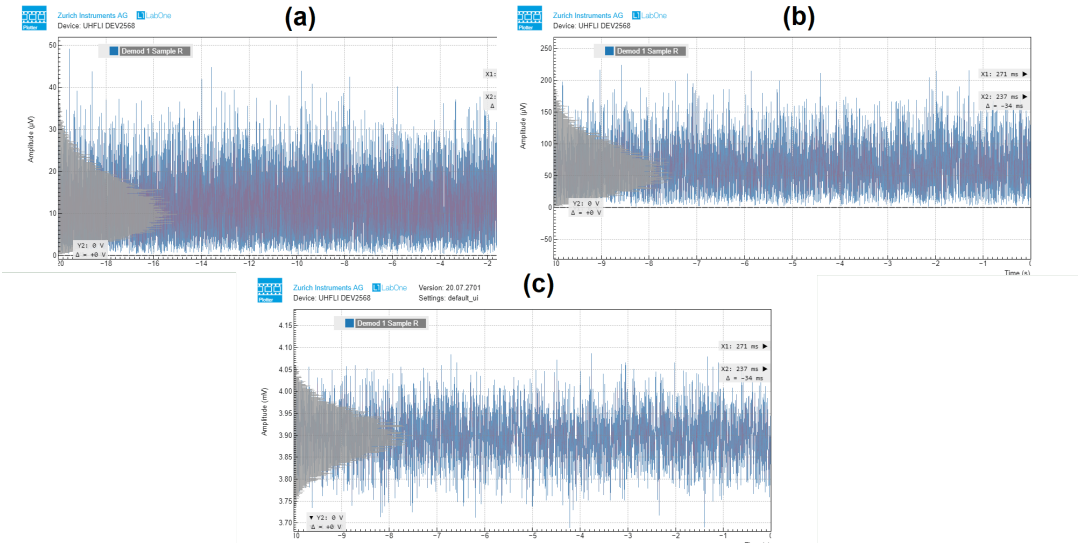

Figure B.1: Time domain response of the circuit's output for gyroscope #3. Results used for Table 5.6. (a) Output with power supply; (b) Output with power supply + carrier wave; (c) Output with the power supply + carrier wave + driving signal.

B.2 MokuLab Phase Sensitive Demodulation for Gyroscope #3

This appendix is an expansion of the results obtained in 5.4 for other devices.The MokuLab Lock In Amplifier was used to demodulate the quadrature signal. A sinusoidal wave of the same frequency as the output of the gyroscope was produced, with a 90° phase shift. It is possible to see in figure B.5 that the amplitude of the sensor's output is $27.92mV$ before any demodulation occurs.

The amplitude of the output reduced 56.3%, from $24.85mV$ to $10.86mV$, but still some quadrature error persists.

For Gyroscope #5, the same principle was applied at exactly the resonant peak ($10.623kHz$, taken from the frequency sweeping measurements).

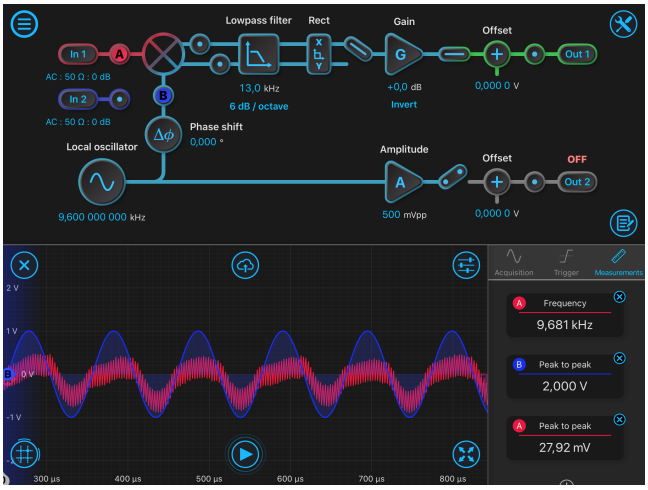

Figure B.2: MokuLab Lock-In Amplifier - (A) Output Signal of the Gyroscope; (B) Local Oscillator at $9.6kHz$ overlying the quadrature signal.

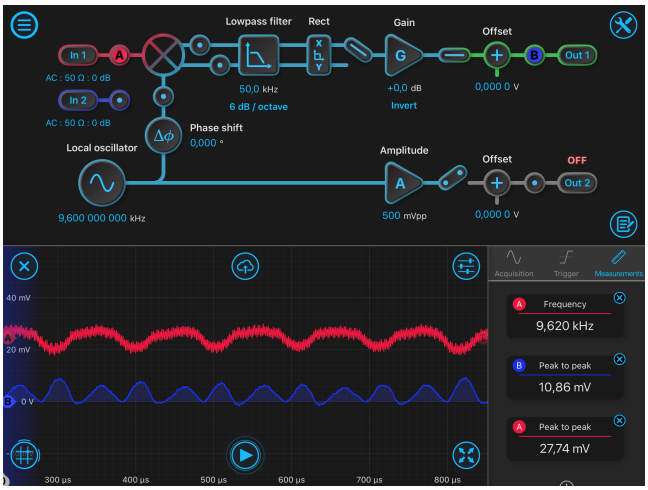

Figure B.3: MokuLab Lock-In Amplifier - (A) Output Signal of the Gyroscope; (B) Output of the gyroscope after the demodulation of the signal

An initial output of $13.54mV$ from the sensor was reduced to $2.69mV$, corresponding to a decrease of 80.13% in output.

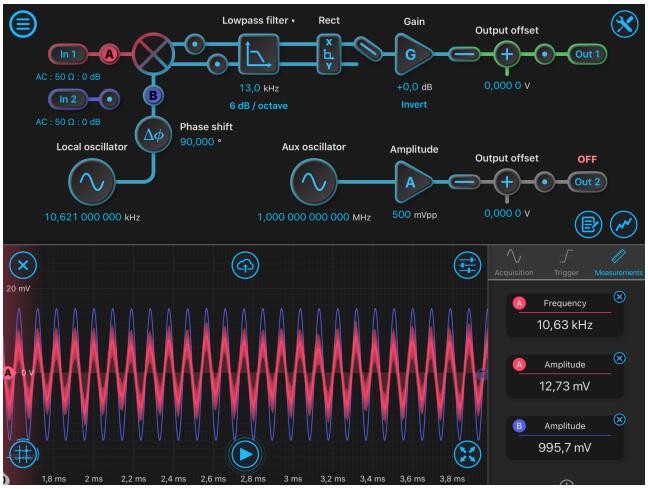

Figure B.4: MokuLab Lock-In Amplifier - (A) Output Signal of the Gyroscope; (B) Local Oscillator at 10.621kHz overlying the quadrature signal.

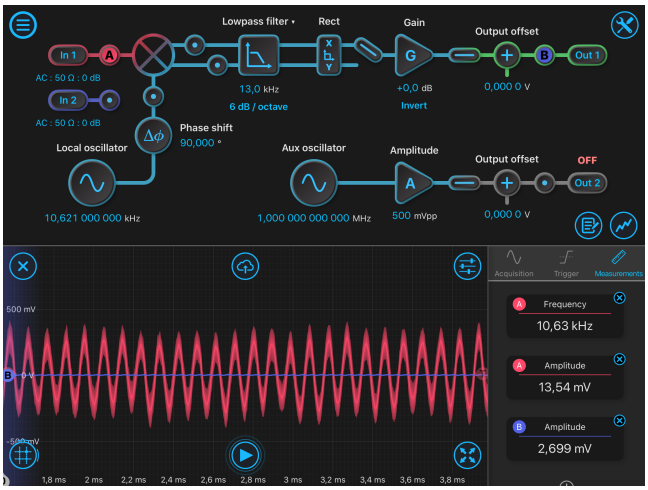

Figure B.5: MokuLab Lock-In Amplifier - (A) Output Signal of the Gyroscope; (B) Local Oscillator at 10.621kHz overlying the quadrature signal.

Appendix

C Phase Measurements

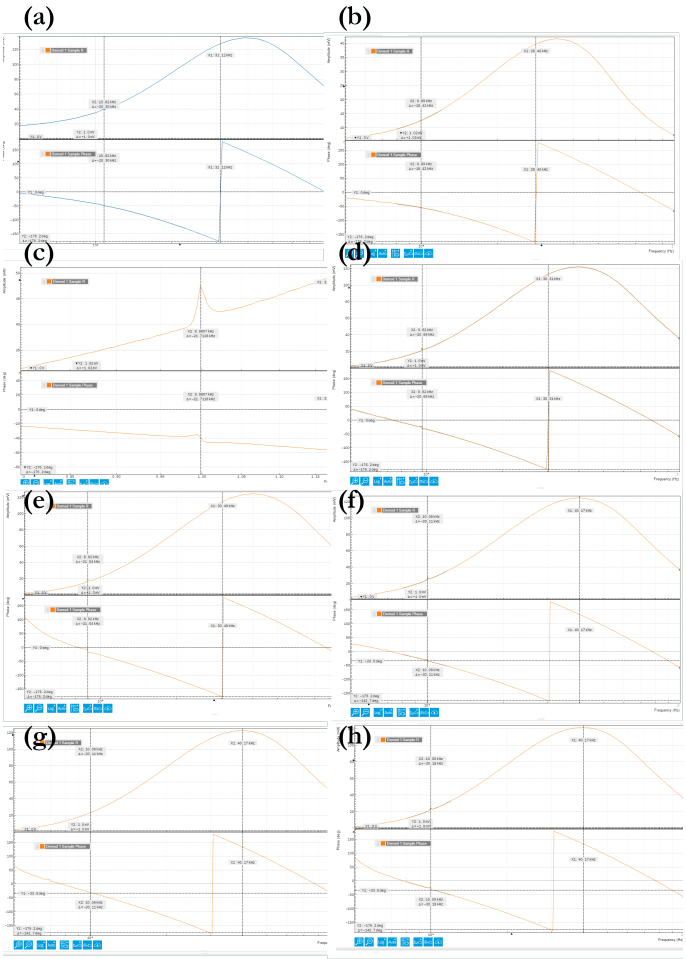

Figure C.1: Phase measurements of the driving mode oscillators. (a) Gyroscope #1 (b) Gyroscope #2 (c) Gyroscope #3 (d) Gyroscope #4 (e) Gyroscope #5 (f) Gyroscope #6 (g) Gyroscope #7 (h) Gyroscope #8

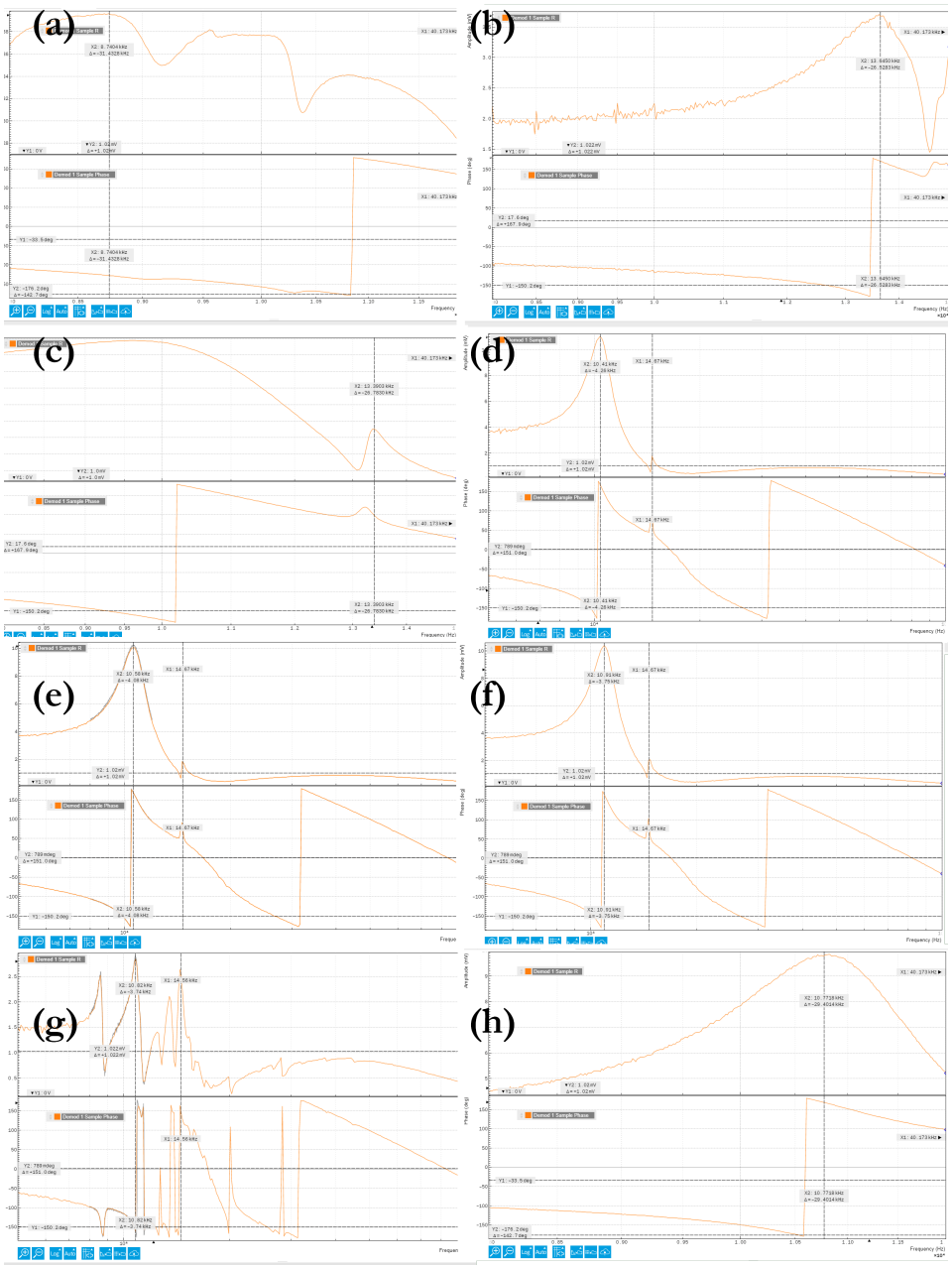

Figure C.2: Phase measurements of the sensing mode oscillators. (a) Gyroscope #1 (b) Gyroscope #2 (c) Gyroscope #3 (d) Gyroscope #4 (e) Gyroscope #5 (f) Gyroscope #6 (g) Gyroscope #7 (h) Gyroscope #8

Appendix

D Capacitive Electrodes

Any two conducting elements that are isolated from each other can make a capacitor. A parallel-plate capacitor consists of two parallel plates of area A, separated by a distance d. When a capacitor is charged with a differential voltage V, its plates get charges of equal magnitude but opposite signs ($-q$ and $+q$). Usually, this value is referred to as Q – although it is the absolute value of the charge on any plate, not the net charge, which is always zero [58]. The amount of charge stored is given by:

$$C = Q/V \tag{D.1}$$

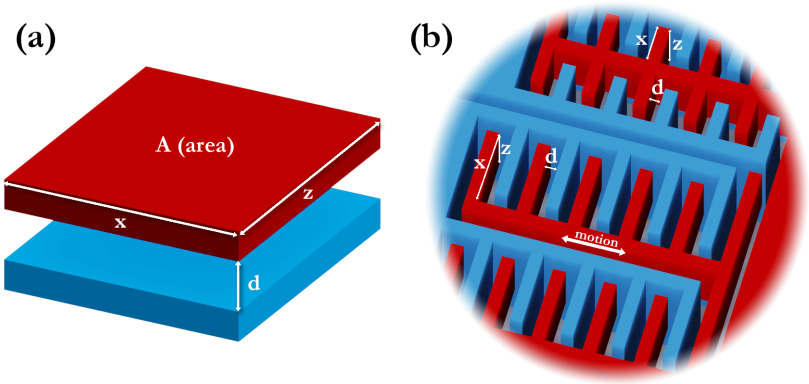

Figure D.1: Capacitive plates example (a) A simple parallel plate capacitor; (b) Structures commonly called comb fingers, in a bulk micromachined vibratory gyroscope, that act as capacitive plates.

The constant C is called capacitance, which depends exclusively on the plates' geometry, position, and material separating them [58]. The SI unit of capacitance is the Farad, which is an enormous unit, meaning that submultiples of it are more commonly used [37].

$$1 farad = 1F = 1 Coloumb/Volt \tag{D.2}$$

Alternatively, the capacitance of a flat capacitor can be given by:

$$C = \frac{\epsilon_0 A}{d} \tag{D.3}$$

Table D.1: Permittivity value

Permittivity	**Value**
ϵ_0 (free space)	8.85×10^{-12} F/m

The equation D.3 is essential when designing capacitive electrodes for sensing applications since the relationship between the area and the distances between the plates will change the measured capacitance value [37].

Annex

I Allan Variance Method

This annex is a complement to Section 5.3.2, working as an theoretical introduction to the Allan Variance method. The explanations presented are based on Koldbæk et. al [59], and the original paper from Allan, D. [46].

The Allan Variance is used to estimate stability due to noise processes. It is defined as one half of the time average of the squares of the differences between consequent readings of the frequency (or phase/amplitude) deviation sampled over the sampling period. A low Allan Variance is a characteristic of an oscillator with good stability over the measured period.

By actuating the driving mode and gathering the output data of a MEMS Gyroscope it is possible to undertake this study.

Considering the output **R** from a sensor sampled in a discrete time interval (sample frequency): the sampled data points are divided into clusters $t = k \times \tau_0$, with $k = 1, 2, 3, \ldots, N$. From **N** consecutive data points gathered with a sample period of τ_0, a finite dataset is gathered.

Having acquired this finite dataset, the next step is to divide the data into clusters with specific lengths: $\tau_0, 2 \times \tau_0, \ldots, M\tau_0$ – with $M < \frac{N}{2}$. **M** refers to the number of data points within each individual cluster, while τ denotes the integration time equal to $M \times \tau_0$. The process of dividing the data into clusters with ever increasing correlation times (τ) is illustrated in figure I.2.

Additionally, associated with each cluster (k), containing M data points, a cluster average $\bar{R}$ is calculated as:

$$\bar{R}(\tau_M) = \frac{1}{M} \sum_{i=1}^{M} R(k+1)M + i \tag{I.1}$$

Here, $k = 1, 2, 3, \ldots, K$ and $K = N/M$. By dividing data into clusters with different τ (integration time) and performing averaging operations, the variance of the cluster averages changes relative to the used correlation time. The bigger the τ time is, the more the deviation diminishes.

By using the overlapping estimator, the data is shifted in each calculation taken into account the cluster average of the samples of the preceding and following clusters. The

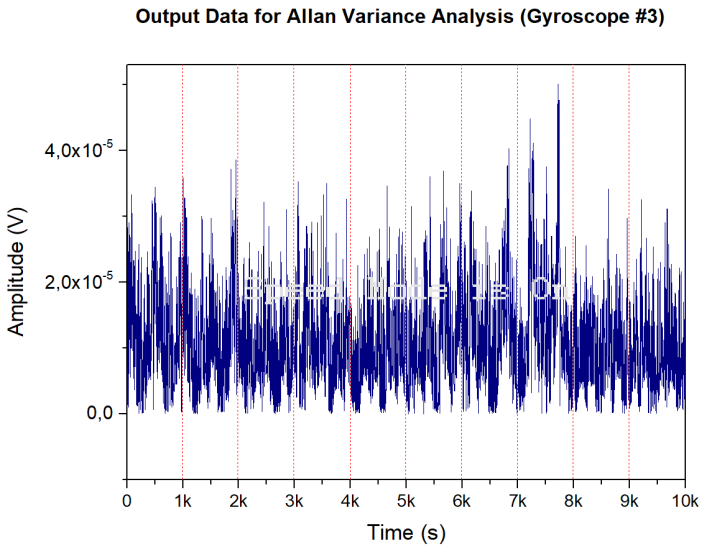

Figure I.1: Illustration of a dataset (partial) used for the Allan Variance calculation. The presented data refers to Gyroscope #3, it was sampled at $f = 800Hz$ (800 samples per second) - resulting in a total of 138240000 data points over $48h$.

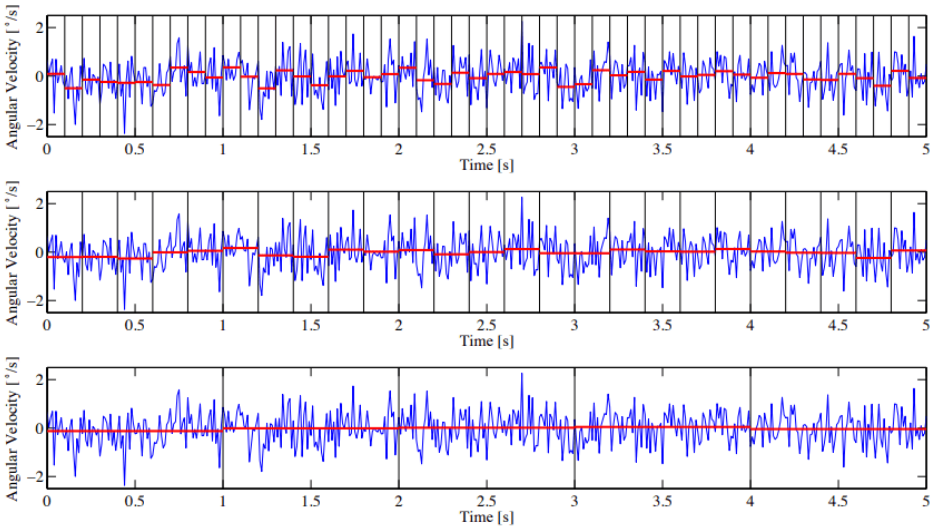

Figure I.2: : Creation of clusters with different integration time - taken from [59]

overlapping estimator is calculated as follows:

$$\sigma_A^2(\tau) = \frac{1}{2(K-1)} \sum_{i=1}^{K-1} (\bar{R}_{k+1}(M) - \bar{R}_k(M))^2 \tag{I.2}$$

Using the Allan Variance with this estimator is the method recommended by IEEE to characterize MEMS Gyroscopes [40].

Having gathered all the data points and performed the calculations expressed above,

the next step is to plot the acquired AV coefficients as a function of the integration time (τ) in a log-log plot.

By examining the slope of the Allan Variance plot, it is possible to identify the magnitude of the different noise ssources present in the captured data. In figure I.3, a standardized Allan Variance plot, containing different noise sources is illustrated. When using real data sampled from a sensor, the transitions and slopes may not present themselves as sharply.

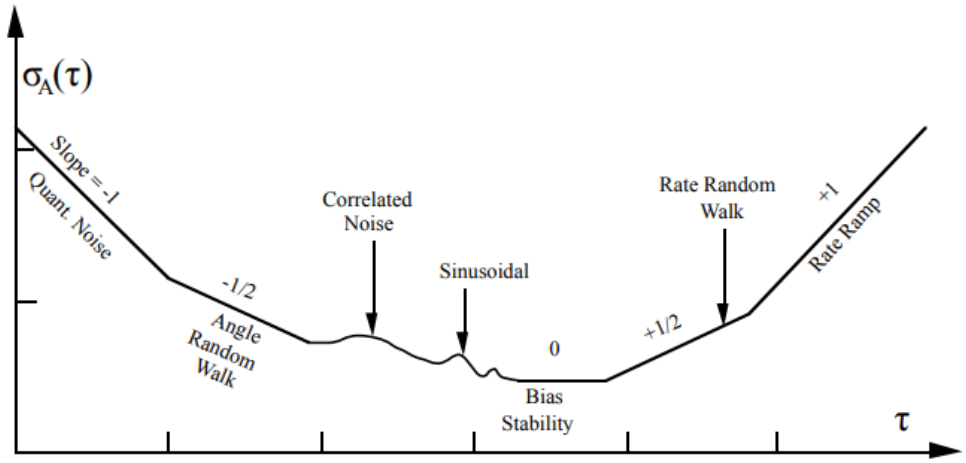

Figure I.3: Sample Plot of Allan Variance Analysis Results - taken from [59]

The typical cluster size τ range can go from several minutes for ARW, to several hours for the Bias Stability, and several days for RRW - taking an integration time of at least 10000s as reported by Lawrence et al. [51].

As explained in Section 5.3.2, three key parameters can be taken from this graph:

- The ARW is a measure of random white noise resulting from the output integration of the stationary gyroscope.
- The RRW coefficient refers to the random walk noise component in the gyroscope rate output. It is usually permanent in nature and are resulting from stochastic noise sources.
- The Bias Stability reflects the output stability over a certain length of time, and is a fundamental performance metric of any MEMS inertial sensor - it is the lowest registered Allan Variance coefficient.

Annex

II Python Scripts

Listagem II.1: Data Treatment Python Script from the UHFLI

```
######## ALLAN VARIANCE PARSER ########

    import pandas as pd

    allan1 = "avar1_g6.txt" #variable to store file #1
    allan2 = "avar2_g6.txt" #variable to store file #2
    allan3 = "avar3_g6.txt" #variable to store file #3

    sample_time = 1/800 # samples per second (Hz) / (Sp/s) zurich instruments

    # Panda datafile setup
    df1 = pd.read_csv(allan1, delimiter = ";")
    df2 = pd.read_csv(allan2, delimiter = ";")
    df3 = pd.read_csv(allan3, delimiter = ";")

    # Gets total rows for each datafile, important for timestep procedure
    total_rows1 = len(df1.index)
    total_rows2 = len(df2.index)
    total_rows3 = len(df3.index)

    #Drops Time Column
    df1.drop(df1.columns[0],axis=1,inplace=True)
    df2.drop(df2.columns[0],axis=1,inplace=True)
    df3.drop(df3.columns[0],axis=1,inplace=True)

    ##### Parsing first file for origin reading #######
    #time1=[0]
    #time_step = 0
```

```
    #for x in range(total_rows1 - 1):
    #     time_step = time_step + sample_time
    #     time1.append(time_step)

    #df1['Time(s)'] = time1

    ##### Parsing second file for origin reading #######

    #time2=[]

    #x=0
    #for x in range(total_rows2):
    #     time_step = time_step + sample_time
    #     time2.append(time_step)
    #df2['Time(s)'] = time2

    #### Outputting ####

    df1.to_csv("output_dataset_gyro6.txt", sep=";", decimal=".",
    index=False, header=False)
    df2.to_csv("output_dataset_gyro6.txt", sep=";", decimal=".",
    mode='a', header=False, index=False)
    df3.to_csv("output_dataset_g6.txt", sep=";", decimal=".",
    mode='a', header=False, index=False)
```

Listagem II.2: Overlapped Allan Variance Algorithm

```
### OVERLAPPED ALLAN VARIANCE ALGORITHM ###

    import allantools
    https://github.com/aewallin/allantools/
    import numpy as np
    import pandas as pd

    data = "output_dataset_gyro6.txt" #open file as dataset
    df = pd.read_csv(data, delimiter = ";")
    dataset = df.to_numpy()
    print(dataset[0])

    # Compute a deviation using the Dataset
    t = np.logspace(0, 5)  # tau values from 1 to 1000
```

```
r = 800  # sample rate in Hz of the input data
(t2, ad, ade, adn)
= allantools.oadev(dataset, rate=r, data_type="phase", taus=t)

# Write results to file

out = pd.DataFrame(list(zip(t2,ad)),
                   columns =['Tau', 'OADEV'])

out.to_csv("output_aovar_gyro_6.txt", sep=";", decimal="."
, index=False, header=False)
```